



TECHNISCHE
UNIVERSITÄT
WIEN

DIPLOMARBEIT

Calculation of Vertex Asymptotics from Local Correlation Functions

Ausgeführt am

Institut für Festkörperphysik
der Technischen Universität Wien

unter der Anleitung von

Univ. Prof. Dipl.-Phys. Dr. rer. nat. Karsten Held

und

Dipl.-Ing. Patrik Gunacker

durch

Josef Kaufmann

Farberweg 28, 6380 St. Johann in Tirol

Datum

Unterschrift

Abstract

The aim of this work is the derivation of a method to compute the high-frequency asymptotics of local two-particle correlation functions. This leads to a substantial improvement regarding the calculation and storage of vertex functions, and allows for a better calculation of physical properties of strongly correlated electron systems.

In Chapter 1 we give an introduction to the Hubbard model and the Anderson impurity model for strongly correlated electron systems, as well as an overview regarding the Green's function and Feynman diagram formalisms of quantum field theory employed in this Thesis. Dynamical mean field theory with continuous-time quantum Monte Carlo (QMC) as an impurity solver is further introduced as a tool to compute local one- and two-particle Green's functions.

In Chapter 2, we derive a procedure to extract the so-called *kernel functions* from local two-particle Green's functions, an efficient parametrization of the high-frequency asymptotics of vertices, and demonstrate its usability by means of analytic calculations in the atomic limit.

In Chapter 3, we present several results obtained by applying our new procedure to QMC data of both a one-band model system and an *ab initio* simulation of SrVO₃ with three bands. It is thereby shown that, compared to conventional methods, the inclusion of vertex asymptotics into various calculations leads to significantly more accurate results regarding both finite-box errors and statistical uncertainties.

Zusammenfassung

Das Ziel dieser Arbeit war es, eine Methode zur Berechnung der Hochfrequenzasymptotik von lokalen Zweiteilchen Green-Funktionen zu finden. Dies führt zu einer wesentlichen Verbesserung der Berechnung und Speicherung der Zweiteilchen Green-Funktionen, die zur Berechnung von Eigenschaften stark korrelierter Elektronensysteme benötigt werden.

In Kapitel 1 werden das Hubbard-Modell und das Anderson-Störstellenmodell für stark korrelierte Elektronensysteme eingeführt. Außerdem wird ein Überblick über den Formalismus der Greenschen Funktionen und Feynman Diagramme gegeben, wie sie in der vorliegenden Arbeit verwendet werden. Als Methode zur Berechnung der lokalen Greenschen Funktionen für ein und zwei Teilchen stellen wir die dynamische Molekularfeldtheorie mit Quanten Monte Carlo (QMC) als Methode zur Lösung des Störstellenproblems vor.

In Kapitel 2 leiten wir eine Methode her, um die sogenannten Kernfunktionen aus Zweiteilchen Green-Funktionen zu berechnen. Auf diese Weise gelingt es uns, die Hochfrequenzasymptotik von Vertizes effizient zu parametrisieren; und wir demonstrieren die Gültigkeit der Methode anhand analytischer Berechnungen im atomaren Limes.

In Kapitel 3 präsentieren wir verschiedene Ergebnisse, die durch Anwendung unserer neuen Methode mit QMC-Daten erhalten wurden. Im Zuge dessen wurden sowohl ein Ein-Band Hubbard-Modell als auch eine Drei-Band *ab initio* Simulation des Materials SrVO_3 untersucht. Dabei zeigen wir, dass, verglichen mit konventionellen Methoden, unser Weg zu Ergebnissen mit verbesserter Genauigkeit führt. Dies betrifft zum einen eine Verbesserung endlicher Summationen mithilfe der Asymptotik und zum anderen eine Reduktion der statistischen Unsicherheit.

Contents

1	Introduction	3
1.1	Model Hamiltonians and interactions	4
1.2	Definition of Green's functions	6
1.3	Properties of Green's functions	7
1.4	Calculation of Green's functions	11
1.5	Continuous-time Quantum Monte Carlo	16
1.6	Two-particle Green's function	21
1.7	Susceptibility	25
2	Vertex asymptotics	31
2.1	Motivation	31
2.2	Derivation	35
2.3	Analytical calculations for the atomic limit	40
3	Applications and results	51
3.1	ED-benchmark: 3D one-band Hubbard model	51
3.2	Multi-band test case: SrVO ₃	63
4	Conclusion and outlook	71
A	Frequency notations	73

Chapter 1

Introduction

There is a variety of phenomena in solid state physics that have their origin in the strong correlation of electrons. Prominent among these are the Mott-Hubbard metal-to-insulator transition [1] or high-temperature superconductivity[2], to name a few. While systems with weaker electronic correlation can be described successfully within density functional theory [3] by assuming the ground state energy to be a functional of the electron density, for strongly correlated systems one has to explicitly deal with the many-body problem posed by the electronic Hamiltonian [4, 5]

$$H = \sum_i \left(-\frac{\nabla_i^2}{2m_e} + V_{\text{ion}}(\mathbf{r}_i) \right) + \frac{1}{2} \sum_{i \neq j}^N \frac{e^2}{|\mathbf{r}_i - \mathbf{r}_j|}. \quad (1.1)$$

Here, the summation in the first term goes over all electrons of the system, ∇_i is the gradient operator with respect to the coordinates of the i -th electron, m_e is the electron mass and $V_{\text{ion}}(\mathbf{r}_i)$ is the ionic potential of the lattice at the position of the i -th electron.

It is impossible to solve the full problem for more than a few particles, but one can model the physical situation in a simpler way. Typically strong correlations between electrons arise when they are well localized. This is the case for partially filled $3d$ and $4f$ shells, in so-called transition metals and rare earths. Here the electrons are most probably found in a small region of space, belonging to a certain atom. Nevertheless, these electrons remain generally quite mobile and can thus “hop” from one atom to another. If two electrons happen to be in the same orbital, which is allowed due to the Pauli principle only when they have different spin, they

are relatively close to each other, giving rise to strong repulsion and thus also to strong correlation.

1.1 Model Hamiltonians and interactions

1.1.1 Hubbard Model

The situation described above is captured in the Hubbard model [6]. By ignoring the atoms that actually constitute the crystal, electrons are considered to “live” on a lattice. They can sit, strongly localized, on a certain site, and move across the lattice by hopping from site to site. The Pauli principle then prohibits other electrons of the same spin to hop to the same site. Thus, one lattice site can be unoccupied, occupied by one electron, or by two electrons of opposite spin. In the latter case, the Hubbard model includes an on-site Coulomb repulsion. Using the formalism of second quantization, the Hamiltonian for this model is

$$H_{\text{Hubbard}} = - \sum_{ij,\sigma} t_{ij} \hat{c}_{i\sigma}^\dagger \hat{c}_{j\sigma} + U \sum_i \hat{n}_{i\uparrow} \hat{n}_{i\downarrow}. \quad (1.2)$$

The constant t_{ij} is called hopping amplitude, U represents the Coulomb interaction. The operator $\hat{c}_{i\sigma}^{(\dagger)}$ annihilates (creates) an electron with spin σ on lattice site i , and $\hat{n}_{i\sigma} = \hat{c}_{i\sigma}^\dagger \hat{c}_{i\sigma}$ is the number operator. Since c and c^\dagger are fermionic operators, they obey the following anticommutation relations:

$$\{c_i, c_j\} = \{c_i^\dagger, c_j^\dagger\} = 0 \quad \text{and} \quad \{c_i, c_j^\dagger\} = \delta_{ij} \quad (1.3)$$

Usually the hopping t_{ij} is restricted to nearest or next-to-nearest neighbour hopping, such that the full sum $\sum_{i,j}$ is reduced to the sum over the considered neighbours, which is often denoted as $\sum_{\langle i,j \rangle}$.

The Hubbard Hamiltonian can be generalized to multiple orbitals or bands and a Kanamori interaction [7] between these, see also Refs. [5, 8]. Using i and j as site

indices, α and β for orbitals, and σ to indicate the spin, we have

$$\begin{aligned}
H_{\text{HK}} = & - \sum_{ij,\alpha,\sigma} t_{ij,\alpha\sigma} \hat{c}_{i\alpha\sigma}^\dagger \hat{c}_{j\alpha\sigma} + U \sum_{i,\alpha} \hat{n}_{i\alpha\uparrow} \hat{n}_{i\alpha\downarrow} \\
& + U' \sum_{i,\alpha \neq \beta} \hat{n}_{i\alpha\uparrow} \hat{n}_{i\beta\downarrow} + (U' - J) \sum_{i,\alpha < \beta, \sigma} \hat{n}_{i\alpha\sigma} \hat{n}_{i\beta\sigma} \\
& - J \sum_{i,\alpha \neq \beta} \hat{c}_{i\alpha\uparrow}^\dagger \hat{c}_{i\alpha\downarrow} \hat{c}_{i\beta\downarrow}^\dagger \hat{c}_{i\beta\uparrow} + J \sum_{i,\alpha \neq \beta} \hat{c}_{i\alpha\uparrow} \hat{c}_{i\alpha\downarrow} \hat{c}_{i\beta\uparrow}^\dagger \hat{c}_{i\beta\downarrow}^\dagger \quad (1.4)
\end{aligned}$$

Here, the Hubbard U represents the intra-orbital Coulomb interaction. The newly introduced parameter U' stands for inter-orbital interaction and J introduces Hund's coupling into the model. A non-vanishing J leads to spin-flips and pair-hopping, which are non-density-density interactions and can be seen in the last line of Eq. (1.4). To achieve a more compact form of the Hubbard-Kanamori Hamiltonian, the parameters U , U' and J are combined to the so-called U-matrix U_{abcd} . Eq. (1.4) then takes the form

$$H = - \sum_{ij,a} t_{ij,a} \hat{c}_{ia}^\dagger \hat{c}_{ja} + \frac{1}{2} \sum_i \sum_{abcd} U_{abcd} \hat{c}_{ia}^\dagger \hat{c}_{ib}^\dagger \hat{c}_{ic} \hat{c}_{id}, \quad (1.5)$$

where the compound indices a , b , c and d were used to denote both spin and orbital degrees of freedom in a compact way. Eq. (1.5) can also describe a more general albeit local interaction, but in this Thesis we restrict ourselves to the Kanamori interaction.

1.1.2 Anderson Impurity Model

If one wants to describe the scattering of electrons at an impurity site inside a metal, another fundamental model of solid states theory is used: the Anderson impurity model [9]. As will be shown later, it is closely related to the Hubbard model, but instead of a lattice, only one impurity site in a non-interacting bath is considered. Electrons can move from the bath to the impurity site and back; this hopping amplitude is often called hybridization. If there are two electrons on the impurity site, they interact just like in the Hubbard model. In order to write down the Hamiltonian, we need to distinguish two types of creation and annihilation operators: $\hat{c}^{(\dagger)}$ annihilates (creates) a bath electron and $\hat{d}^{(\dagger)}$ annihilates (creates)

an electron at the impurity site. The Anderson Hamiltonian then reads

$$\begin{aligned}
H_{AIM} = & \underbrace{\frac{1}{2} \sum_{abcd} U_{abcd} \hat{d}_a^\dagger \hat{d}_b^\dagger \hat{d}_c \hat{d}_d - \sum_{\alpha} \varepsilon_{\alpha} (\hat{n}_{\alpha\uparrow} + \hat{n}_{\alpha\downarrow})}_{H_{loc}} \\
& + \underbrace{\sum_{\mathbf{ka}} \epsilon_{\mathbf{ka}} \hat{c}_{\mathbf{ka}}^\dagger \hat{c}_{\mathbf{ka}}}_{H_{bath}} + \underbrace{\sum_{\mathbf{kab}} (V_{\mathbf{kab}} \hat{c}_{\mathbf{ka}}^\dagger \hat{d}_b + V_{\mathbf{kab}}^* \hat{d}_b^\dagger \hat{c}_{\mathbf{ka}})}_{H_{hyb} = \tilde{H}_{hyb} + \tilde{H}_{hyb}^\dagger} \quad (1.6)
\end{aligned}$$

Here, we have used the impurity occupation number operator $\hat{n}_{\alpha\sigma} \equiv \hat{n}_a = \hat{d}_a^\dagger \hat{d}_a$ and compound indices $a = (\alpha, \sigma)$. The bath dispersion $\epsilon_{\mathbf{ka}}$ is the Fourier transform of the hopping amplitude of the bath electrons, where \mathbf{k} stands for the momentum. $V_{\mathbf{kab}}$ denotes the hybridization amplitude for an electron being transferred from the impurity state b to the bath state \mathbf{ka} , and ε_{α} is the local one-particle potential of the impurity orbital α .

1.2 Definition of Green's functions

In the context of many-body systems, a one-particle Green's function describes the reaction of a system of many particles, if one particle is added or removed for a certain time, which leads to the definition of the causal one-particle Green's function

$$\begin{aligned}
G_C^{(1)}(\vec{r}_1, t_1; \vec{r}_2, t_2) &= -i \langle \mathcal{T} \psi(\vec{r}_1, t_1) \psi^\dagger(\vec{r}_2, t_2) \rangle \\
&= -i \langle \psi(\vec{r}_1, t_1) \psi^\dagger(\vec{r}_2, t_2) \rangle \Theta(t_1 - t_2) + i \langle \psi^\dagger(\vec{r}_2, t_2) \psi(\vec{r}_1, t_1) \rangle \Theta(t_2 - t_1). \quad (1.7)
\end{aligned}$$

For a more compact form, in the first equality we made use of the Wick time-ordering operator \mathcal{T} . In the second equality, the time ordering is written explicitly. The two terms have different sign due to the fermion exchange relation. The operators $\psi^{(\dagger)}(\vec{r}, t) \equiv e^{-iHt} \psi^{(\dagger)}(\vec{r}, 0) e^{iHt}$ annihilate (create) a fermion at position \vec{r} and time t . $\langle \dots \rangle$ denotes the expectation value $\text{Tr}(e^{-\beta H} \dots) / \text{Tr}(e^{-\beta H})$, which reduces to the ground state expectation value $\langle \text{GS} | \dots | \text{GS} \rangle$ for $T = 0$. However, to treat finite temperatures $T > 0$, it is more convenient to perform a Wick rotation $t \rightarrow -i\tau$, $\tau \in \mathbb{R}$ to negative imaginary times instead of real times. This has the effect that

the time evolution e^{-iHt} becomes a purely real operator $e^{\tau H}$ and can be combined with the Boltzmann factor $e^{-\beta H}$. We then obtain the so-called temperature Green's function

$$G_{ij}^{(1)}(\tau_1, \tau_2) = - \left\langle \mathcal{T} \psi_i(\tau_1) \psi_j^\dagger(\tau_2) \right\rangle. \quad (1.8)$$

For convenience, the space-coordinates \vec{r}_1 and \vec{r}_2 have been absorbed into indices i and j , which can also refer to lattice sites. In general, these indices contain the spin and orbital associated to the operator as well. Analogously to the one-particle Green's function, it is possible to define the n -particle Green's function

$$G_{i_1, \dots, i_{2n}}^{(n)}(\tau_1, \dots, \tau_{2n}) = (-1)^n \left\langle \mathcal{T} \prod_{j=1}^n \psi_{i_{2j-1}}(\tau_{2j-1}) \psi_{i_{2j}}^\dagger(\tau_{2j}) \right\rangle. \quad (1.9)$$

For notational reasons, spin and orbital degrees of freedom have been subsumed in compound indices i_1, \dots, i_{2n} together with lattice site indices. Since we usually consider electrons in a periodic lattice, it is advantageous to switch over from real to reciprocal space by means of a Fourier transform, i. e. in three dimensions

$$\psi^{(\dagger)}(\mathbf{r}, \tau) = \frac{1}{(2\pi)^3} \int d^3k c_{\mathbf{k}}^{(\dagger)}(\tau) e^{(-)i\mathbf{k}\mathbf{r}}. \quad (1.10)$$

The one-particle Green's function becomes then

$$G_{a\mathbf{k}b\mathbf{k}'}^{(1)}(\tau_1, \tau_2) = - \left\langle \mathcal{T} c_{a\mathbf{k}}(\tau_1) c_{a\mathbf{k}}^\dagger(\tau_2) \right\rangle \delta_{ab} \delta_{\mathbf{k}\mathbf{k}'}, \quad (1.11)$$

where a and b are now compound indices containing the quantum numbers of spin and orbital.

1.3 Properties of Green's functions

Green's functions have several important properties that are used many times throughout this thesis. Therefore, a brief summary will be given here. For a more detailed treatment, we refer the reader to the standard literature [10, 11, 12, 13] and in particular to Refs. [14, 15].

1.3.1 Time domain

The usage of imaginary time has an important consequence for the time domain, on which the Green's function is defined. Writing down explicitly the expectation value of Eq. (1.9) leads to

$$G_{i_1, \dots, i_{2n}}^{(n)}(\tau_1, \dots, \tau_{2n}) \propto \sum_m e^{(\tau_1 - \tau_{2n} - \beta)E_m} \langle m | \psi_{i_1} e^{-\tau_1 H} \dots e^{\tau_{2n} H} \psi_{i_{2n}}^\dagger | m \rangle, \quad (1.12)$$

with a chosen time-ordering of $\tau_1 > \dots > \tau_{2n}$. Here, we have used the eigenbasis $|m\rangle$ and the spectrum of eigenvalues E_m of the Hamiltonian H . Since, in general, neither the number of eigenstates nor the eigenvalues themselves have an upper bound, it is necessary to require that the difference between the greatest and smallest time argument be smaller than the inverse temperature:

$$\tau_1 - \tau_{2n} < \beta \quad (1.13)$$

1.3.2 Antiperiodicity

The definition of a Green's function in Eq. (1.9) contains a trace of time-ordered operators and a factor $e^{-\beta H}$ that can be combined with a time evolution operator to obtain the following form:

$$\begin{aligned} \text{Tr} \left[e^{-\beta H} e^{\tau_1 H} \psi_{i_1} e^{-\tau_1 H} \psi_{i_2}^\dagger(\tau_2) \dots \psi_{i_{2n}}^\dagger(\tau_{2n}) \right] \\ = \text{Tr} \left[e^{(\tau_1 - \beta)H} \psi_{i_1} e^{-(\tau_1 - \beta)H} e^{-\beta H} \psi_{i_2}^\dagger(\tau_2) \dots \psi_{i_{2n}}^\dagger(\tau_{2n}) \right] \end{aligned}$$

The cyclic property of the trace allows us to move the first operator to the end of the sequence, such that we get

$$\text{Tr} \left[e^{-\beta H} \psi_{i_2}^\dagger(\tau_2) \dots \psi_{i_{2n}}^\dagger(\tau_{2n}) e^{(\tau_1 - \beta)H} \psi_{i_1} e^{-(\tau_1 - \beta)H} \right].$$

Now we use the commutation relation for fermionic creation and annihilation operators to perform the $2n - 1$ commutations that shift ψ_{i_1} to the left of ψ_{i_2} again. This changes the sign of the trace and we obtain

$$G_{i_1 \dots i_{2n}}^{(n)}(\tau_1, \dots, \tau_{2n}) = -G_{i_1 \dots i_{2n}}^{(n)}(\tau_1 - \beta, \dots, \tau_{2n}). \quad (1.14)$$

Similar reasoning leads to

$$G_{i_1 \dots i_{2n}}^{(n)}(\tau_1, \dots, \tau_{2n}) = -G_{i_1 \dots i_{2n}}^{(n)}(\tau_1, \dots, \tau_{2n} + \beta). \quad (1.15)$$

The above two equations mean that fermionic Green's functions are *anti-periodic*. This has the very important consequence that we can express a Green's function as a Fourier series in which only odd coefficients are non-zero. The respective frequencies are called *fermionic Matsubara frequencies*

$$\nu_n = \frac{\pi}{\beta}(2n + 1), \quad n \in \mathbb{Z}. \quad (1.16)$$

With this, we can write

$$G_{i_1 \dots i_{2n}}^{(n)}(\tau_1, \dots, \tau_{2n}) = \frac{1}{\beta^n} \sum_{j_1 \dots j_{2n} \in \mathbb{Z}} e^{-i\nu_{j_1}\tau_1 + i\nu_{j_2}\tau_2 - \dots + i\nu_{j_{2n}}\tau_{2n}} G_{i_1 \dots i_{2n}}^{(n), \nu_{j_1}, \dots, \nu_{j_{2n}}}. \quad (1.17)$$

1.3.3 Time translation invariance and energy conservation

The trace of a product of operators is invariant with respect to cyclic permutations. Hence, putting the last time evolution operator to the beginning of the operator sequence is equivalent to shifting time by $-\tau_{2n}$, if the Hamiltonian is time independent. This means that Green's functions are invariant with respect to time translation, such that

$$G_{i_1 \dots i_{2n}}^{(n)}(\tau_1, \tau_2 \dots \tau_{2n}) = G_{i_1 \dots i_{2n}}^{(n)}(\tau_1 - \tau_{2n}, \tau_2 - \tau_{2n}, \dots, 0) \quad (1.18)$$

Applying the Fourier transformation to this time-shifted Green's function leads to

$$\sum_{k=1}^n \nu_{2k} = \sum_{k=1}^n \nu_{2k-1}, \quad (1.19)$$

where frequencies with even index are associated with creation operators and odd with annihilators. Here the index is not used in the context of definition (1.16), but rather to denote the operator it is associated with. Relation 1.19 means that the energy of the system is conserved and has the important consequence that the n -particle Green's function effectively depends not on $2n$, but only on $2n - 1$ Matsubara frequencies. In the case of the two-particle Green's function, it

is therefore conventional to use, instead of four fermionic, two fermionic and one bosonic Matsubara frequency that satisfy condition (1.19). Various choices exist and will be discussed in Appendix A.

1.3.4 Crossing symmetry

A system of indistinguishable fermions has the property that upon exchange of two particles the wave function of the system changes its sign. This corresponds to the Pauli principle and in second quantization is captured by the fermionic anticommutation relations (1.3). Thus, also the two-particle Green's function, as defined in Eq. (1.9) changes the sign if creation or annihilation operators are exchanged [14]:

$$G_{ijkl}^{(2)}(\tau_1, \tau_2, \tau_3, \tau_4) = -G_{kjil}^{(2)}(\tau_3, \tau_2, \tau_1, \tau_4) = G_{klij}^{(2)}(\tau_3, \tau_4, \tau_1, \tau_2) = -G_{ilkj}^{(2)}(\tau_1, \tau_4, \tau_3, \tau_2) \quad (1.20)$$

The same relations are valid in Matsubara representation with $\nu_1 \dots \nu_4$ instead of $\tau_1 \dots \tau_4$.

1.3.5 SU(2) symmetry

In general, an n -particle Green's function has $2n$ spin and $2n$ orbital indices. However, many systems are invariant under SU(2) transformations. This symmetry can be broken, for example, by application of a magnetic field. In the presence of SU(2) symmetry, certain spin components are identical. Since these identities hold for arbitrary orbital components, the orbital indices are dropped in the following to keep the notation simple.

In an SU(2)-symmetric system, the one-particle Green's function is spin-diagonal and, due to spin conservation, it is sufficient to write only one spin-index:

$$G_{\sigma\sigma}^{(1)} \equiv G_{\sigma}^{(1)} = G_{\sigma'}^{(1)}. \quad (1.21)$$

The two-particle Green's function has four spin indices and therefore, a priori, 16 possible spin-components. Spin conservation reduces this number to six, such that it is of advantage to introduce the shorthand notation $G_{\sigma\sigma'} \equiv G_{\sigma\sigma\sigma'\sigma}$ and $G_{\sigma\sigma'}^- \equiv G_{\sigma\sigma'\sigma'\sigma}$. The six components mentioned above, $G_{\uparrow\uparrow}$, $G_{\uparrow\downarrow}$, $G_{\downarrow\downarrow}$, $G_{\downarrow\uparrow}$, $G_{\downarrow\uparrow}$ and

$G_{\downarrow\downarrow}$, are connected by the following SU(2) symmetry relations [14]:

$$G_{\uparrow\uparrow}^{(2)} = G_{\downarrow\downarrow}^{(2)} \quad (1.22)$$

$$G_{\uparrow\downarrow}^{(2)} = G_{\downarrow\uparrow}^{(2)} \quad (1.23)$$

$$G_{\uparrow\uparrow}^{(2)} = G_{\uparrow\downarrow}^{(2)} + G_{\downarrow\uparrow}^{(2)} \quad (1.24)$$

The first two of the above identities follow from flipping all spins. The third one can be obtained by rotating the spins by an angle of $\pi/2$.

1.4 Calculation of Green's functions

1.4.1 Perturbation theory

Expectation values in the interaction picture

For interacting systems, it is convenient to split the full many-body Hamiltonian H , as defined in Eq. (1.1), into a non-interacting kinetic part H_0 and an interaction term H_V . Applying the Fourier transformation (1.10) and using second quantization, the kinetic energy reads

$$H_0 = \frac{1}{(2\pi)^3} \int \sum_{\sigma,\alpha} d^3\mathbf{k} \epsilon_{\alpha\sigma\mathbf{k}} c_{\alpha\sigma\mathbf{k}}^\dagger c_{\alpha\sigma\mathbf{k}}, \quad (1.25)$$

where the sum is taken over the spin (σ) and orbital (α) degrees of freedom. The interaction Hamiltonian, for simplicity without spin and orbital dependence, is of the form

$$H_V = \int \frac{d^3k}{(2\pi)^3} \int \frac{d^3k'}{(2\pi)^3} \int \frac{d^3q}{(2\pi)^3} c_{\mathbf{k}+\mathbf{q}}^\dagger c_{\mathbf{k}'-\mathbf{q}}^\dagger \frac{V(\mathbf{q})}{2} c_{\mathbf{k}'} c_{\mathbf{k}}. \quad (1.26)$$

If there was no interaction, the Green's function would be given by

$$G_{0,\alpha\sigma}(\mathbf{k}, i\nu) = \frac{1}{i\nu - \epsilon_{\mathbf{k}\alpha\sigma}}. \quad (1.27)$$

This is the Green's function of the Schrödinger equation for a free particle. The above splitting of the Hamilton operator corresponds to the interaction picture,

which can be defined by the following equations:

$$S(\tau) = e^{\tau H_0} e^{-\tau H} = e^{\tau H_0} U_S(\tau) \quad (1.28)$$

$$\mathcal{O}_I(\tau) \equiv e^{\tau H_0} \mathcal{O}_S e^{-\tau H_0} = U_I(\tau) \mathcal{O}_H(\tau) U_I^\dagger(\tau) \quad (1.29)$$

$$|\psi_I(\tau)\rangle = U_I(\tau) |\psi\rangle = e^{\tau H_0} |\psi_S(\tau)\rangle \quad (1.30)$$

Subscripts I , H and S denote the interaction- Heisenberg- and Schrödinger picture of time evolution. Computing $\partial S(\tau)/\partial\tau$ leads to a Schrödinger equation for the interaction-picture time-evolution operator $S(\tau)$ with the solution

$$S(\tau) = \mathcal{T} e^{-\int_0^\tau d\tau' H_V^I(\tau')} = \sum_{n=0}^{\infty} \frac{(-1)^n}{n!} \int_0^\beta d\tau_1 \cdots \int_0^\beta d\tau_n \mathcal{T} H_V^I(\tau_1) \cdots H_V^I(\tau_n). \quad (1.31)$$

In the computation of expectation values, the operator $e^{-\beta H}$ plays an important role. By means of Eq. (1.28) it can be expressed as $e^{-\beta H_0} S(\beta)$. This allows for rewriting the interacting expectation value in terms of non-interacting quantities:

$$\langle \mathcal{O} \rangle = \frac{1}{Z} \text{Tr} [e^{-\beta H} \mathcal{O}] = \frac{1}{Z} \text{Tr} [e^{-\beta H_0} S(\beta) \mathcal{O}] = \langle S(\beta) \mathcal{O} \rangle_0 \quad (1.32)$$

Inserting the S -matrix (1.31) leads to a perturbation expansion in H_V . It is possible to apply this in the calculation of the partition function Z and Green's functions, where it leads to non-interacting expectation values of products of an even number of operators. For such terms, Wick's theorem [16] provides a useful method of simplification: A non-interacting product of n creation- and annihilation operators can be decomposed into a sum of all contractions into creator-annihilator pairs, for example

$$\begin{aligned} \left\langle \mathcal{T} c_{\mathbf{k}+\mathbf{q}}^\dagger c_{\mathbf{k}'-\mathbf{q}}^\dagger \frac{V(\mathbf{q})}{2} c_{\mathbf{k}'} c_{\mathbf{k}} \right\rangle_0 &= \frac{V(\mathbf{q})}{2} \left[\langle \mathcal{T} c_{\mathbf{k}} c_{\mathbf{k}}^\dagger \rangle_0 \langle \mathcal{T} c_{\mathbf{k}'} c_{\mathbf{k}'}^\dagger \rangle_0 \delta_{\mathbf{q}0} \right. \\ &\quad \left. - \langle \mathcal{T} c_{\mathbf{k}+\mathbf{q}} c_{\mathbf{k}+\mathbf{q}}^\dagger \rangle_0 \langle \mathcal{T} c_{\mathbf{k}} c_{\mathbf{k}}^\dagger \rangle_0 \delta_{\mathbf{k},\mathbf{k}'-\mathbf{q}} \right], \quad (1.33) \end{aligned}$$

which is the first-order term of the expansion of the partition function Z . By applying the definition of the Green's function in Eq. (1.11) we can further simplify the two-operator expectation values.

of *irreducibility*. A diagram that does not fall apart after cutting a propagator is called (one-particle) *irreducible*.

The above reasoning suggests that we may collect all irreducible diagrams to one entity Σ , sum up all iterations and thereby obtain the full *interacting* Green's function $\longleftarrow (G)$:

$$\begin{aligned} \longleftarrow &= \text{---} \longleftarrow \text{---} + \text{---} \longleftarrow \text{---} \textcircled{\Sigma} \text{---} \longleftarrow \text{---} + \\ &+ \text{---} \longleftarrow \text{---} \textcircled{\Sigma} \text{---} \textcircled{\Sigma} \text{---} \longleftarrow \text{---} + \dots \end{aligned} \quad (1.38)$$

The sum of all irreducible diagrams, Σ , is called *self energy*. After a simple reformulation of the above equation, we arrive at the *Dyson equation*,

$$\longleftarrow = \text{---} \longleftarrow \text{---} + \text{---} \longleftarrow \text{---} \textcircled{\Sigma} \longleftarrow \quad (1.39)$$

or

$$G_{\mathbf{k}}(\tau) = G_{\mathbf{k}}^0(\tau) + \int_0^\beta d\tau_1 \int_0^\beta d\tau_2 G_{\mathbf{k}}^0(\tau_1) \Sigma_{\mathbf{k}}(\tau_2 - \tau_1) G_{\mathbf{k}}(\tau - \tau_2). \quad (1.40)$$

This is greatly simplified by Fourier transformation [5], because then the convolution integral becomes an ordinary multiplication

$$G_{\mathbf{k}}(i\nu) = G_{\mathbf{k}}^0(i\nu) + G_{\mathbf{k}}^0(i\nu) \Sigma_{\mathbf{k}}(i\nu) G_{\mathbf{k}}(i\nu) \quad (1.41)$$

such that we get the following simple relation for the self-energy:

$$\Sigma_{\mathbf{k}}(i\nu) = [G_{\mathbf{k}}^0(i\nu)]^{-1} - [G_{\mathbf{k}}(i\nu)]^{-1}. \quad (1.42)$$

Combining Eqs. (1.42) and (1.27) leads to a more explicit form of the interacting Green's function:

$$G_{\mathbf{k}}(i\nu) = [i\nu - \epsilon_{\mathbf{k}} - \Sigma_{\mathbf{k}}(i\nu)]^{-1}. \quad (1.43)$$

1.4.2 Dynamical mean field theory

Ultimately, we are interested in calculating interacting Green's functions for arbitrary parameters and also real materials. A very important method to achieve

this is the *dynamical mean field theory* or DMFT. It is based on the fact that the Hubbard model (eq. 1.2) stays non-trivial even at the limit of infinite space dimensions d or coordination number \mathcal{Z} , if the hopping parameter t is properly scaled [17]:

$$t = \frac{t^*}{\sqrt{\mathcal{Z}}}, \quad (1.44)$$

where t^* stays constant when the number of neighbours increases. Since $\langle c_{i\sigma}^\dagger c_{j\sigma} \rangle$ (or the one-particle Green's function) scales in the same way as t , and the sum in Eq. (1.2) contains \mathcal{Z} terms, the hopping term of the Hubbard Hamiltonian stays constant in the limit of infinite dimensions. The interaction term contains only local terms, hence it does not need any scaling. An important consequence of the scaling of the Green's function is that non-local contributions to the self-energy vanish in the limit of infinite dimensions (see, e. g. [18]).

It was subsequently shown [19] that the Hubbard model can be mapped onto a single-impurity Anderson model. This can be done in a self-consistent way by requiring that the self-energy has to be the same in the impurity problem and in the lattice problem.

The self consistency cycle can be summarized as follows [5]:

1. As a start, choose a trivial local self-energy.
2. Calculate the local Green's function by integrating the Dyson equation over the first Brillouin zone:

$$G(i\omega) = \frac{1}{V_{BZ}} \int_{BZ} d^3\mathbf{k} \left[\underbrace{i\omega + \mu - \epsilon(\mathbf{k})}_{G_0(\mathbf{k}, i\omega)} - \Sigma(\omega) \right]^{-1} \quad (1.45)$$

3. Define the effective non-interacting Green's function $\mathcal{G}_0(i\omega)$ of the auxiliary impurity model:

$$\mathcal{G}_0(i\omega) = \left([G(i\omega)]^{-1} + \Sigma(i\omega) \right)^{-1} \quad (1.46)$$

4. Now the impurity problem has to be solved for its interacting Green's function $G(i\omega)$. There exist several methods to solve the impurity problem, among them the exact diagonalization (ED) algorithm [20] and quantum Monte Carlo (QMC) algorithms. The latter will be described in Sec. 1.5.

5. The last step of the self-consistency cycle is inverting the Dyson equation in order to obtain a new self-energy:

$$\Sigma(i\omega) = [\mathcal{G}_0]^{-1} - [G(i\omega)]^{-1} \quad (1.47)$$

With this new self-energy, steps 2. to 5. are repeated until a convergence criterion is met.

1.5 Continuous-time Quantum Monte Carlo

As mentioned above, in DMFT it is necessary to solve the auxiliary Anderson impurity problem. To this end, several methods have been proposed, and the choice of the solver may depend on the parameters of the problem. When it comes to low temperatures and multi-orbital systems, the method of choice is a quantum Monte Carlo (QMC) algorithm.

The first QMC algorithm that was widely applied for solving the Anderson impurity model, was the Hirsch-Fye method [21], which uses imaginary-time discretization. This leads to errors, in particular for resolving steep features of the imaginary-time Green's function at low temperatures, which are of great interest. These issues are largely mitigated by *continuous-time* QMC (CT-QMC) methods, which are today's state-of-the-art [22].

The basic idea common to all CT-QMC methods is the expansion of the expectation value into a diagrammatic series, similarly as discussed in Sec. 1.4.1. There are various ways to split the Hamiltonian of the AIM in Eq. (1.6), and thus also various possibilities to define a free system and a perturbation term. One way is to use an expansion in the local interaction $\sum U_{ijkl} d_i^\dagger d_j^\dagger d_k d_l$, which results in the *interaction expansion* algorithm (CT-INT) [23]. For strong interactions U , and more general interactions at low temperatures, it turns out that one better uses the hybridization term as the perturbation for the expansion, resulting in the *hybridization expansion* algorithm (CT-HYB) [24, 25].

For the problems considered in this work, it is most advantageous to use a CT-HYB solver. Thus, all DMFT and two-particle calculations in this work were done by CT-HYB using the package `W2DYNAMICS` [26]. For this reason, a brief description

of the hybridization-expansion CT-QMC is given here, mostly following Refs. [22, 27].

1.5.1 Hybridization Expansion

As already indicated by its name, the hybridization expansion takes H_{hyb} as a perturbation, whereas $H_{loc} + H_{bath}$ are treated exactly. Thus, the partition function in the interaction picture reads

$$Z = \sum_{k=0}^{\infty} \frac{(-1)^k}{k!} \int_0^\beta d\tau_1 \dots \int_0^\beta d\tau_n \text{Tr} \left[\mathcal{T} e^{-\beta(H_{bath} + H_{loc})} H_{hyb}(\tau_1) \dots H_{hyb}(\tau_n) \right]. \quad (1.48)$$

Since H_{hyb} contains one term that creates and one term that annihilates an impurity electron, only terms with the same number of \tilde{H}_{hyb} and \tilde{H}_{hyb}^\dagger can contribute to the trace, which also implies an even expansion order $n = 2k$. We define now the bath partition function as

$$Z_{bath} = \text{Tr} \left[\mathcal{T} e^{-\beta H_{bath}} \right] \quad (1.49)$$

and the hybridization function for the non-interacting bath as

$$\Delta_{ab}(\tau) = \sum_{\vec{k}i} \frac{V_{\vec{k}ia}^* V_{\vec{k}ib}}{e^{\epsilon_i \beta} + 1} \times \begin{cases} -e^{-\epsilon_i(\tau-\beta)}, & 0 < \tau < \beta, \\ e^{-\epsilon_i \tau}, & -\beta < \tau < 0. \end{cases} \quad (1.50)$$

These definitions allow for rewriting the bath-part of the trace in Eq. (1.48) as the determinant of a matrix of hybridization functions $\Delta_{ab}(\tau)$, called hybridization matrix Δ .

$$Z = Z_{bath} \sum_{k=0}^{\infty} \int_0^\beta d\tau_1 \sum_{a_1} \dots \int_0^\beta d\tau_{2k} \sum_{a_{2k}} \text{Tr}_d \left[d_{a_{2k}}(\tau_{2k}) \dots d_{a_1}^\dagger(\tau_1) \right] \det \Delta. \quad (1.51)$$

The remaining trace now goes over the subspace spanned by the local operators. The integration in Eq. (1.51) over all orders k and all imaginary times τ_i is done by CT-QMC.

In Monte Carlo (MC), the expectation value

$$\langle A \rangle = \frac{\int_{\mathcal{C}} d\mathbf{x} \mathcal{A}(\mathbf{x}) p(\mathbf{x})}{\int_{\mathcal{C}} d\mathbf{x} p(\mathbf{x})} \quad (1.52)$$

of an observable A is given by

$$\langle A \rangle_{MC} = \frac{1}{M} \sum_{i=1}^M \mathcal{A}(\mathbf{x}_i). \quad (1.53)$$

The sample configurations \mathbf{x}_i should be a Markov chain belonging to the weight $p(\mathbf{x})$. Transitions from a configuration \mathbf{x} to a configuration \mathbf{y} are done with a probability W_{xy} that is the product of a proposal probability W_{xy}^{prop} and an acceptance probability W_{xy}^{acc} . The latter is determined by the acceptance ratio

$$r_{xy} = \frac{p(\mathbf{y})W_{yx}^{\text{prop}}}{p(\mathbf{x})W_{xy}^{\text{prop}}} \quad (1.54)$$

via the Metropolis-Hastings algorithm [28, 29] as

$$W_{xy}^{\text{acc}} = \min [1, R_{xy}]. \quad (1.55)$$

In CT-HYB, a configuration is a set of k annihilation operators d and k creation operators d^\dagger . Each operator has a certain time argument τ_i and a flavor index a , denoting spin and orbital. The weight of such a configuration is given by the integrand (including the infinitesimals $d\tau$) of Eq. (1.51); and also the transition probabilities can be computed from it. A transition between two measurement configurations is done by updating the operator sequence by a certain number of moves, in order to obtain uncorrelated configurations. There are several kinds of updates (moves). The most basic ones, necessary for ergodicity, are operator pair insertions and removals. Further moves, such as insertion and removal of antisegments and time-shifting operators, reduce the autocorrelation time and thereby increase the performance of the computation.

The local trace can be visualized in switchboard pictures (Fig. 1.1) and for density-density interactions also in segment pictures (Fig. 1.2).

It is possible to draw also the hybridization of the local operators with the bath (please recall that every operator d is connected to an operator c^\dagger and vice versa) by connecting every creator with every annihilator by so-called *hybridization lines*. In order to avoid the fermionic sign problem, we restrict ourselves to flavor-diagonal hybridization functions. Such a case is shown in Fig. 1.3.

Having indicated how to sample the partition function of a system, we now turn to

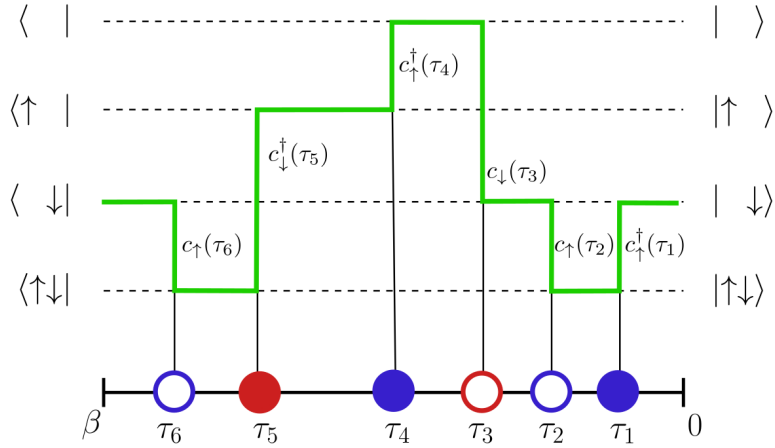


Figure 1.1: Switchboard picture of a sample configuration. Filled and empty circles represent creation and annihilation operators, respectively. The spin orientations \uparrow and \downarrow are encoded by blue and red color. Taken from Ref. [27].

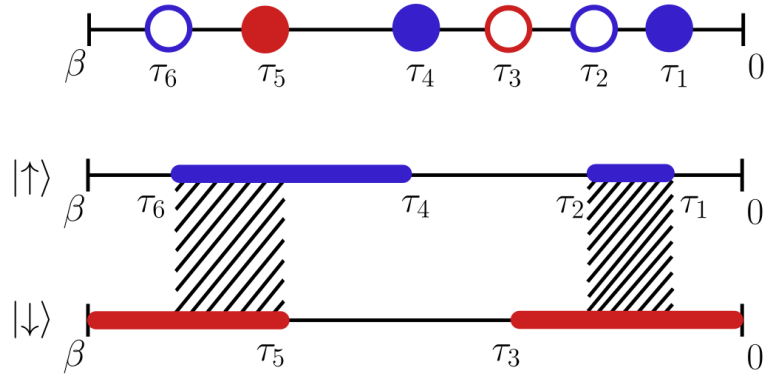


Figure 1.2: Segment picture of the same operator configuration as in Fig. 1.1. Taken from Ref. [27].

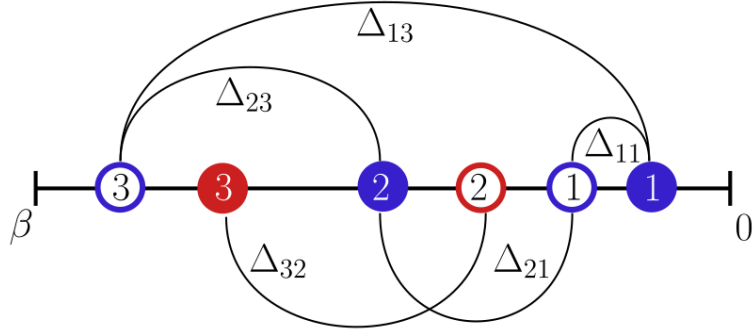


Figure 1.3: Hybridization lines for the same operator configuration as in Fig. 1.1. The hybridization function is assumed to be flavor-diagonal. Taken from Ref. [27].

the task of computing Green’s functions, because this is necessary in DMFT, and also for the calculation of vertices and their asymptotics. The latter is the main topic of this Thesis. The diagrammatic series expansion of the Green’s function is almost identical to the expansion of the partition function, the only difference consisting in the presence of an additional local creator-annihilator pair that does not hybridize. Therefore, one way of calculating Green’s functions is removing the hybridization from one operator pair of the Z-expansion and removing the corresponding row and column of the hybridization matrix. However, in the multi-orbital case with general interactions, it is necessary to use the worm sampling method, since not all two-particle vertices can be obtained by removing hybridization lines [30].

1.5.2 Worm Sampling

In Metropolis-Hastings MC, one samples the probability density function in the denominator of the expectation value (1.52). Thus, applied to the thermal expectation value of quantum field theory, one samples the partition function Z and constructs estimators for the observables from it.

The idea of worm sampling is now to directly sample the perturbation series expansion of the expectation value of the observable. This means that the configuration space \mathcal{C} is enlarged, for instance from \mathcal{C}_Z to $\mathcal{C}_Z \oplus \mathcal{C}_G$ if the Green’s function is measured [30, 22]. To achieve that the sampling takes place in both spaces, a number of additional moves is required to switch between spaces, grant for ergodicity and

minimize autocorrelation times.

To get from partition function space to a Green's function space, it is necessary to insert a pair of non-hybridizing, so-called worm-operators into the operator sequence. To get back to partition function space, such a pair has to be removed. Once being in a worm space, in order to do a proper random walk, it must be possible to do the same updates as in the partition function space. Furthermore, it was shown [30] that the autocorrelation time can be significantly reduced by introducing worm shift/replacement moves, in which one of the worm operators is swapped with a hybridizing operator.

The worm sampling method makes it possible to measure one- and two-particle Green's functions as well diagrammatically improved estimators for the self energy and the two-particle vertex [31]. For this work, it is of particular importance that worm sampling also provides the possibility to compute Green's functions with pairs of operators at equal times, which are important for the vertex asymptotics.

1.6 Two-particle Green's function

Motivated by the knowledge that physically important quantities like susceptibilities involve the calculation of two-particle quantities, we start our investigation by applying the perturbation and diagrammatic techniques developed previously to the two-particle Green's function. (The link to physical susceptibilities will be established later on, in Sec. 1.7.) In the way shown in Sec. 1.4.1, the two-particle Green's function reads

$$G_{\mathbf{k}\mathbf{k}'\mathbf{q}}(\tau_1, \tau', \tau'') = \frac{1}{\langle S(\beta) \rangle_0} \sum_{n=0}^{\infty} \frac{(-1)^n}{n!} \int_0^\beta d\tau_1 \cdots \int_0^\beta d\tau_n \langle \mathcal{T} H_V^I(\tau_1) \cdots H_V^I(\tau_n) c_{\mathbf{k}}(\tau) c_{\mathbf{k}-\mathbf{q}}^\dagger(\tau') c_{\mathbf{k}'-\mathbf{q}}(\tau'') c_{\mathbf{k}'}^\dagger \rangle_0. \quad (1.56)$$

As already done above for the one-particle Green's function, it is possible to expand also the two-particle Green's function into an infinite series of Feynman diagrams. The contribution in zeroth order is just

$$G_{\mathbf{k}}^0(\tau - \tau') G_{\mathbf{k}'}^0(\tau'') \delta_{\mathbf{q}0} - G_{\mathbf{k}}^0(\tau) G_{\mathbf{k}-\mathbf{q}}^0(\tau'' - \tau') \delta_{\mathbf{k}\mathbf{k}'} \quad (1.57)$$

or diagrammatically

$$\begin{array}{ccc}
\begin{array}{c} \tau \\ \vdots \\ \mathbf{k} \uparrow \\ \vdots \\ \tau' \end{array} & \begin{array}{c} 0 \\ \vdots \\ \delta_{\mathbf{q}0} \\ \vdots \\ \mathbf{k}' \downarrow \\ \vdots \\ \tau'' \end{array} & - & \begin{array}{c} \tau \dashleftarrow \mathbf{k} \dashrightarrow 0 \\ \delta_{\mathbf{k}\mathbf{k}'} \\ \tau' \dashrightarrow \mathbf{k} - \mathbf{q} \dashrightarrow \tau'' \end{array}
\end{array} \quad (1.58)$$

Regarding diagrams of higher order, we get self-energy corrections for the diagrams of Eq. (1.58), but also other terms occur. For example, the following first-order terms, for simplicity Fourier-transformed and with four-vector notation $k = (\nu, \mathbf{k})$,

$$\begin{array}{ccc}
\begin{array}{c} k_1 \quad k_4 \\ \dashrightarrow \quad \dashleftarrow \\ \delta_{k_1+k_3, k_2+k_4} \\ \vdots \\ \delta_{k_1+k_3, k_2+k_4} \\ \dashleftarrow \quad \dashrightarrow \\ k_2 \quad k_3 \end{array} & V(k_1 - k_4)/2, & \begin{array}{c} k_1 \quad k_3 \\ \swarrow \quad \searrow \\ V(k_1 - k_2)/2 \\ \delta_{k_1+k_3, k_2+k_4} \\ \swarrow \quad \searrow \\ k_2 \quad k_4 \end{array}
\end{array} \quad (1.59)$$

are connected diagrams. Hence, they contribute to the so-called *connected* part or vertex correction of the two-particle Green's function. Inclusion of higher orders leads, similar as in the one-particle case, to dressing of the lower-order parts, the concatenation of lower-order parts and new irreducible parts.

This can be summarized (and generalized to more degrees of freedom) by the following equation:

$$\begin{aligned}
G_{abcd}^{(2)}(\tau_1, \tau_2, \tau_3, \tau_4) &= \langle T c_a(\tau_1) c_b^\dagger(\tau_2) \rangle \langle T c_c(\tau_3) c_d^\dagger(\tau_4) \rangle \\
&\quad - \underbrace{\langle T c_a(\tau_1) c_d^\dagger(\tau_4) \rangle \langle T c_c(\tau_3) c_b^\dagger(\tau_2) \rangle}_{\chi_{abcd}(\tau_1, \tau_2, \tau_3, \tau_4)} + \chi_{abcd}^{\text{conn}}(\tau_1, \tau_2, \tau_3, \tau_4)
\end{aligned} \quad (1.60)$$

Here, the compound indices a , b , c , and d include, besides spin and orbital, also the momentum. It has to be kept in mind that, whenever two-particle quantities are written with four frequency/momentum indices, energy/momentum conservation requires $k_1 + k_3 = k_2 + k_4$. A clear graphical representation of Eq. (1.60) can be achieved by Fourier transforming it according to Eq. (1.17). Heuristically, we can take Eq. (1.58), with the free propagators replaced by dressed ones, to account for the disconnected parts and adapt the diagram of Eq. (1.59) but with a box of

Feynman diagrams F instead of the bare interaction line:

$$\begin{aligned}
 & \text{Diagram with vertices } a, b, c, d \text{ and external legs } k_1, k_2, k_3, k_4 \text{ is } G_{abcd}^{(2)} \\
 & = \text{Diagram with two vertical lines } G_a(k_1) \text{ and } G_c(k_4) \text{ and interaction } \beta \delta_{\nu_1 \nu_2} \delta_{ab} \delta_{cd} \\
 & \quad - \beta \delta_{\nu_1 \nu_4} \delta_{ad} \delta_{bc} + \text{Diagram with square } -F_{abcd} \text{ and external legs } G_a(k_1), G_b(k_2), G_c(k_3), G_d(k_4) \\
 & \quad \underbrace{\hspace{10em}}_{\chi_0} \quad \underbrace{\hspace{10em}}_{\chi^{\text{conn}}} \\
 & \hspace{15em} \underbrace{\hspace{15em}}_{\chi_{abcd}}
 \end{aligned}
 \tag{1.61}$$

In these equations, latin indices denote compound indices of both spin and orbital degrees of freedom, but the momentum is now incorporated in the four-vectors k_i . If we deal with local quantities, as is the case quite often, we write only frequency arguments ν_i instead four-vector arguments k_i . The newly introduced χ is called *generalized susceptibility*, it will be subject of Sec. 1.7.

1.6.1 Reducibility and parquet equation

Whereas the disconnected parts of the two-particle Green's function, which consist of products of one-particle Green's functions, have a relatively simple structure, the connected part χ^{conn} contains more diagrams and it is thus worth having a closer look on it. First, we notice that any diagram contributing to the connected part must have four outer "legs" (i.e. one-particle Green's functions). An example for this can be seen already in Eq. (1.59). Since those legs are common to all terms, it is reasonable to remove ("amputate") them before proceeding with the further investigation. What remains after this, is the full (reducible) two-particle vertex F . Here, a diagram is called *two-particle reducible*, if it can be separated into disconnected diagrams by cutting two Green's function lines. So far, this definition is analogue to the one-particle case, but it is now possible to make a further classification, because there are three distinct ways to separate two pairs of legs by cutting two lines. As visualized in Fig. 1.4, we can separate (i) (1,2) from (3,4), (ii)

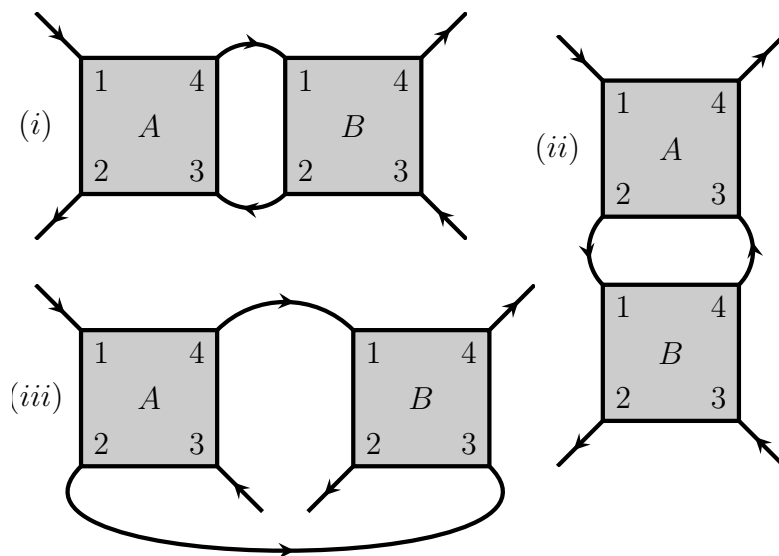


Figure 1.4: Two-particle diagrams, reducible in the longitudinal particle-hole channel (top left), transversal particle-hole channel (right) and particle-particle channel (bottom left).

(1,4) from (2,3) and (iii) (1,3) from (2,4). Such diagrams are called reducible in the (i) particle-hole (ii) transverse particle-hole and (iii) particle-particle channel. This classification is captured in the so-called parquet equation:

$$F = \Lambda + \Phi_{ph} + \Phi_{\overline{ph}} + \Phi_{pp} \quad (1.62)$$

Λ is the fully irreducible vertex and Φ_ℓ is the reducible vertex in channel ℓ . All quantities in the parquet equation have four flavour and three frequency/momentum indices. They have been omitted in the above equation for the sake of simplicity.

1.6.2 Bethe-Salpeter equations

Since there are three distinct kinds of reducibility in the two-particle case, there are also three different *irreducible vertices*, that can be formally obtained from the parquet equation as $\Gamma_\ell = F - \Phi_\ell$, with $\ell \in \{ph, \overline{ph}, pp\}$. Now we can construct the full vertex as a concatenation of irreducible vertices in a given channel. In the

ph-channel, such a “ladder” would be

$$\begin{aligned}
 \leftarrow \boxed{F} \rightarrow &= \leftarrow \boxed{\Gamma} \rightarrow + \leftarrow \boxed{\Gamma} \rightarrow \leftarrow \boxed{\Gamma} \rightarrow + \\
 &+ \leftarrow \boxed{\Gamma} \rightarrow \leftarrow \boxed{\Gamma} \rightarrow \leftarrow \boxed{\Gamma} \rightarrow + \dots \quad (1.63)
 \end{aligned}$$

Similar as in deriving the Dyson equation, the infinite summation above can be reformulated to

$$F = \Gamma_\ell + \Gamma_\ell (GG)_\ell F, \quad (1.64)$$

which is called *Bethe-Salpeter equation*. Although all indices were omitted here for the sake of clarity, the objects are still matrices with respect to Matsubara frequencies and spin/orbital degrees of freedom. Furthermore, a multiplication of two matrices in fermionic frequencies is defined as

$$(AB)_{\nu\nu'} \equiv \frac{1}{\beta} \sum_{\nu_1} A_{\nu\nu_1} B_{\nu_1\nu'}. \quad (1.65)$$

By a channel-specific choice of the bosonic frequency, the Bethe-Salpeter equations decouple with respect to the bosonic frequency and there exist linear combinations (“channels”) of the vertices that enable for spin-diagonalization, see Sec. 1.7.1.

1.7 Susceptibility

In Eqs. (1.60) and (1.61), the generalized susceptibility was introduced:

$$\chi_{abcd}(k_1, k_2, k_3, k_4) = \langle \mathcal{T} c_a(k_1) c_b^\dagger(k_2) c_c(k_3) c_d^\dagger(k_4) \rangle - \langle \mathcal{T} c_a(k_1) c_b^\dagger(k_2) \rangle \langle \mathcal{T} c_c(k_3) c_d^\dagger(k_4) \rangle \quad (1.66)$$

Here it is clearly visible that the susceptibility can be interpreted as the *correlation* of the propagation of two particles. In Eq. (1.66) the susceptibility can equivalently be defined in space and (imaginary) time, instead of momentum and Matsubara

frequencies. In terms of the full vertex F and the “bubble” χ_0 it is¹

$$\chi^\ell = \chi_0^\ell - \chi_0^\ell F \chi_0^\ell \quad (1.67)$$

with $\ell \in \{ph, \overline{ph}, pp\}$. The Bethe-Salpeter equation can now be rewritten in terms of the generalized susceptibility χ instead of the full vertex F :

$$\chi^\ell = \chi_0^\ell - \chi_0^\ell \Gamma_\ell \chi^\ell \quad (1.68)$$

In the form given above, the Bethe-Salpeter equations couple the different spin components of the vertex functions and susceptibilities. In the particle-hole channel, a decoupling, or spin-diagonalization, can be obtained by considering the following linear combinations of vertex functions:

$$X_d = X_{\uparrow\uparrow} + X_{\uparrow\downarrow}, \quad (1.69)$$

$$X_m = X_{\uparrow\uparrow} - X_{\uparrow\downarrow}, \quad (1.70)$$

where d and m stand for density and magnetic channel, respectively. The symbol X serves as a placeholder to emphasize that the above definitions are commonly used for various two-particle quantities, such as e.g. Γ , F , or χ .

1.7.1 Physical susceptibility

In linear response theory, the susceptibility describes the response of a system to an external perturbation. More precisely, it describes how a perturbation due to an external field $a(t)$, coupling to an operator A , influences the expectation value of an observable B :

$$\langle B(t) \rangle_V - \langle B \rangle_0 = \int_{-\infty}^{\infty} dt' \chi_{BA}(t-t') a(t'). \quad (1.71)$$

The susceptibility χ_{BA} is given by the Kubo-Nakano formula

$$\chi_{BA}(t-t') = -\frac{1}{i\hbar} \Theta(t-t') \langle [B(t), A(t')] \rangle_{V=0}. \quad (1.72)$$

¹ This result can be viewed as an analogy to the Dyson equation for the interacting one-particle Green's function $G = G_0 + G_0 \Sigma G$.

In imaginary time τ this takes the form

$$\chi_{BA}(\tau) = \langle T_\tau B(\tau) A(0) \rangle. \quad (1.73)$$

There are various kinds of susceptibilities, but here only two examples will be given, since they are of importance for this work. Due to energy conservation, it is usual to write generalized susceptibilities with one bosonic and two fermionic frequency indices in a channel-specific notation, e. g. $\chi^{\nu\nu'\omega} \equiv \chi^{\nu(\nu-\omega)(\nu'-\omega)\nu'}$ in the particle-hole channel. A more detailed treatment regarding frequency notations is given in Appendix A.

Charge (density-density) susceptibility

Setting both operators A and B in Eq. (1.73) to the density operator $n = \sum_\sigma c_\sigma^\dagger c_\sigma$ yields the so-called charge (or density-density) susceptibility, that can also be obtained from the generalized susceptibility via summation over the fermionic frequencies of the generalized susceptibility in the density channel that was defined in Eq. (1.69):

$$\chi_d^\omega = \frac{1}{\beta^2} \sum_{\nu\nu'} \underbrace{(\chi_{\uparrow\uparrow}^{\nu\nu'\omega} + \chi_{\uparrow\downarrow}^{\nu\nu'\omega})}_{\chi_d^{\nu\nu'\omega}} \quad (1.74)$$

Spin (magnetic) susceptibility

If we choose both A and B to be spin operators, e. g. $A = B = S_z = \sum_{\tau\tau'} c_\tau^\dagger \sigma_{\tau\tau'}^z c_\tau$, we get the spin (or magnetic) susceptibility, which corresponds to the magnetic channel as defined in Eq. (1.70):

$$\chi_m^\omega = \frac{1}{\beta^2} \sum_{\nu\nu'} \underbrace{(\chi_{\uparrow\uparrow}^{\nu\nu'\omega} - \chi_{\uparrow\downarrow}^{\nu\nu'\omega})}_{\chi_m^{\nu\nu'\omega}} \quad (1.75)$$

1.7.2 Non-local susceptibilities in DMFT

We have seen in Sec. 1.4.2 that in DMFT it is possible to exactly solve the Hubbard model in the limit of infinite space dimensions or for a lattice, where each site has infinitely many neighbouring sites. Real systems are, however, two- or three-dimensional and the lattice sites have a finite number of neighbours at a certain

distance. In this case, the DMFT solution can only constitute an approximation, consisting in the neglect of non-local correlations. Although there is a huge amount of phenomena that can be accounted for by local correlations only, it is desirable to have methods that go beyond this limitation.

To this end, a variety of methods has been developed, but here we will only briefly show how to compute non-local susceptibilities after a DMFT calculation, which actually is the first step of the ladder version of the dynamical vertex approximation (DVA) [32]. There, one assumes the irreducible vertex Γ_{ph} to be purely local. Non-locality is then introduced by building ladder diagrams with non-local Green's functions. In contrast to the full, parquet-based dynamical vertex approximation that is based on a purely local Λ , only ladder diagrams are built, typically with Γ_{ph} or $\Gamma_{\overline{ph}}$. This restriction is justified if the leading instability of the system is known a priori. But the vertex functions are also important for calculating susceptibilities in DMFT, such as the charge and magnetic susceptibility.

To this end, the local vertex Γ_r (with $r \in \{d, m\}$) is calculated from the DMFT susceptibilities by inversion of Eq. (1.68):

$$\Gamma_r = [\chi^r]^{-1} - [\chi_0^r]^{-1} \quad (1.76)$$

On the other hand, we may write down the general non-local Bethe-Salpeter equation for the ph -channel, with suppressed frequency dependence, but explicit momentum dependence.

$$\chi^{r, \mathbf{k}\mathbf{k}'\mathbf{q}} = \chi_0^{r, \mathbf{k}\mathbf{k}'\mathbf{q}} - \sum_{\mathbf{k}_1\mathbf{k}_2} \chi_0^{r, \mathbf{k}\mathbf{k}_1\mathbf{q}} \Gamma_r^{\mathbf{k}_1\mathbf{k}_2\mathbf{q}} \chi^{r, \mathbf{k}_2\mathbf{k}'\mathbf{q}} \quad (1.77)$$

Whereas the matrix multiplications in the above equation do not include spin degrees of freedom due to the spin-diagonalized Bethe-Salpeter equations in the density and magnetic channel, they still involve the (suppressed) fermionic frequency indices. The assumption of a local vertex Γ means that every matrix element $\Gamma^{\mathbf{k}_1\mathbf{k}_2\mathbf{q}}$ has the same value, only the frequency dependence is still present. As a consequence, the matrix multiplications in Eq. (1.77) are simplified to ordinary multiplications in k -space. The quantity of interest is the k -summed susceptibility $\chi^{\mathbf{q}} = \sum_{\mathbf{k}\mathbf{k}'} \chi^{\mathbf{k}\mathbf{k}'\mathbf{q}}$, for which we obtain

$$\chi^{r, \mathbf{q}} = \chi_0^{r, \mathbf{q}} - \chi_0^{r, \mathbf{q}} \Gamma_r \chi^{r, \mathbf{q}} \quad (1.78)$$

and thus

$$\chi^{r,\mathbf{q}} = (\mathbf{1} + \chi_0^{r,\mathbf{q}}\Gamma_r)^{-1}\chi_0^{r,\mathbf{q}}. \quad (1.79)$$

Now we just have to insert the DMFT vertex from Eq. (1.76) to get the desired result.

The matrix inversion in Eq. (1.79) has to be done with respect to fermionic frequency and orbital index. As recently shown [33], for numerical reasons it is more stable to express the irreducible vertex Γ by the reducible F , due to possible divergencies in the former quantity.

Chapter 2

Vertex asymptotics

2.1 Motivation

The calculation of many desired quantities in quantum field theory requires operations with infinite matrices in Matsubara space, for example summations over all frequencies as in the calculation of physical from generalized susceptibilities, or matrix inversions as in the calculation of irreducible vertices. In both cases, the problem boils down to the knowledge of the full vertex on a large box. Although it is obviously not possible to keep in memory infinite vertices, we are nevertheless interested in getting sufficiently large ones with a reasonably low statistical error. The direct calculation of full two-particle quantities on large frequency boxes by CT-HYB is infeasible for two main reasons: First the time to make enough measurements for achieving sufficient statistical accuracy is far too long, and second the required hard-disk space quickly grows to enormous values. Especially for multi-orbital vertices this can become a major bottleneck.

Looking for better alternatives, it is an obvious step to closer investigate the asymptotic behaviour of the full two-particle vertex.¹ This was done before for the irreducible vertex Γ_{ph} in the particle hole channel at $\omega_{ph} = 0$ [34] and for the full vertex F in the one-band case [35, 36]. In this work, both approaches are combined, such that we can obtain multi-orbital vertex functions F at asymptotic values of any frequency.

¹On the one-particle level, the asymptotical structure of the self-energy has been successfully exploited.

From the fact that the physical susceptibility must be finite² and go to zero for larger values of the bosonic frequency ω , we infer that also the generalized susceptibility must approach zero for large values of any of its frequency arguments,

$$\lim_{\nu_i \rightarrow \infty} \chi^{\nu_1 \nu_2 \nu_3 \nu_4} = 0 \quad \forall i \in \{1, 2, 3, 4\}, \quad (2.1)$$

otherwise the frequency summation in the calculation of the physical susceptibility would not converge. The same argument is valid also for the connected part of the susceptibility only. We already saw that

$$\chi^{\text{conn}, \nu_1 \nu_2 \nu_3 \nu_4} \propto G^{\nu_1} G^{\nu_2} F^{\nu_1 \nu_2 \nu_3 \nu_4} G^{\nu_3} G^{\nu_4},$$

and therefore we may draw conclusions for the asymptotic full vertex F from the behaviour of the generalized susceptibility at high frequencies: To guarantee the fulfillment of condition (2.1), the vertex must not grow at high frequencies, because the one-particle Green's function decays only as $1/\nu$.

Terms that do not vanish at high frequencies are thus either totally frequency-independent, or depend on differences, such as $(\nu_i - \nu_j)^{-1}$. The latter will result in a contribution that is constant along $\nu_i = \nu_j$ and decays in other directions.

In order to actually compute the asymptotics, we want to identify which diagrams exhibit a dependence on frequency differences. This can be done by looking at the Fourier phase:

$$\phi(\nu_1, \nu_2, \nu_3, \nu_4) = \nu_1 \tau_1 - \nu_2 \tau_2 + \nu_3 \tau_3 - \nu_4 \tau_4. \quad (2.2)$$

By setting, for instance, $\tau_1 = \tau_2 = \tau$ and $\tau_3 = \tau_4 = \tau'$, we get a phase $\phi(\nu_1 - \nu_2, \nu_3 - \nu_4)$ in the exponential of Eq. (1.17) for $n = 2$, which depends only on frequency differences. Together with the energy conservation condition $\nu_1 + \nu_3 = \nu_2 + \nu_4$ the phase can be simplified to

$$\phi(\nu_1 - \nu_2) = (\nu_1 - \nu_2)(\tau - \tau'). \quad (2.3)$$

Please note that the difference $\nu_1 - \nu_2$ confers to ω_{ph} as defined in Eq. (A.3) in the appendix, and the other possible choices of equal-time pairs analogously lead to ω_{ph}^- and ω_{pp} . Choosing only one equal-time pair, for example $\tau_1 = \tau_2 = \tau$, $\tau_3 = \tau'$

²We do not consider cases, where vertex divergencies occur due to phase transitions.

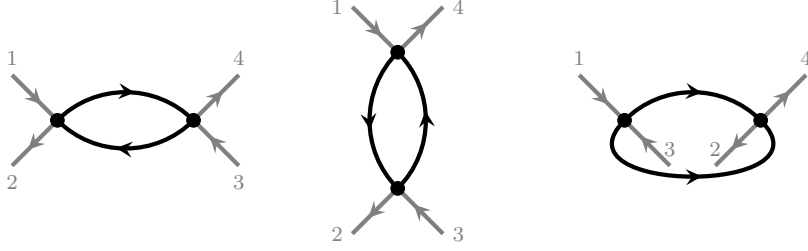


Figure 2.1: Lowest-order diagrams that depend only on one bosonic Matsubara frequency. Note that the propagators already include self-energy corrections. Gray lines denote amputated legs and are there just to indicate the direction of the arrows. From left to right, they correspond to the longitudinal particle-hole channel, the transversal particle-hole channel and the particle-particle channel, in which they are irreducible.

and $\tau_4 = \tau''$, the phase becomes instead

$$\phi(\nu_1 - \nu_2, \nu_3) = (\nu_1 - \nu_2)(\tau - \tau') + \nu_3(\tau - \tau''), \quad (2.4)$$

thus depending on one bosonic and one fermionic Matsubara frequency. The number of choices of equal-time pairs is reduced from 6 to 3 by time reversal symmetry. Diagrammatically, equal-time pairs arise from pairs of propagator-endpoints that belong to one interaction line (or rather dot, in the case of local interaction), which we assume to be instantaneous here. The above findings now allow us to draw diagrams of the perturbation series for the asymptotic vertex F^{asympt} .

- The frequency-independent term can originate only from the simplest possible diagram, a bare interaction U .
- The lowest-order diagrams (in terms of dressed one-particle propagators) depending on one bosonic frequency only are shown in Fig. 2.1.
- The lowest-order contributions that depend on one bosonic and one fermionic frequency are shown in Fig. 2.2.
- All diagrams that do not have two points forced to equal time cannot depend on a frequency difference and, hence, vanish for high values of any of the four fermionic frequencies ν_i . Some diagrams of fourth order, which is the lowest order contributing to this class, are shown in Fig. 2.3.

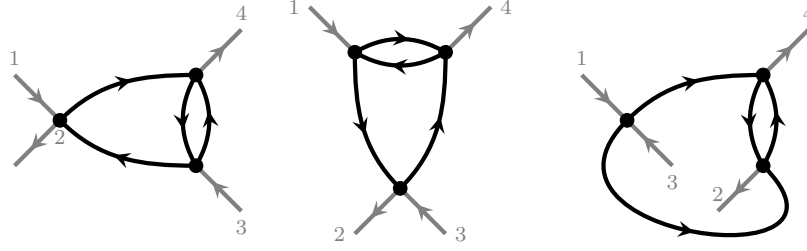


Figure 2.2: Lowest-order diagrams that depend on one bosonic and one fermionic Matsubara frequency. They are called “eye”-diagrams. From left to right, they correspond to the longitudinal particle-hole channel, the transversal particle-hole channel and the particle-particle channel. They are reducible in these three channels, respectively.

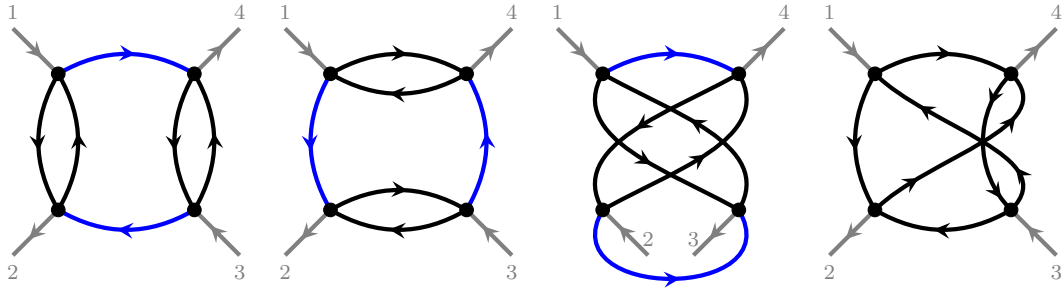


Figure 2.3: The first three diagrams are leading-order diagrams of the strongly decaying (not asymptotic) part of the reducible vertices. The lines that have to be cut to divide the diagrams in two disconnected parts are drawn in blue. The rightmost diagram is fully irreducible.

It does not lead to any new insights to draw diagrams with higher-order vertex corrections, but we note that such corrections will not change the reducibility class of the diagrams. This now leads to an important observation: Except for the frequency-independent background U , the asymptotic vertex consists exclusively of *reducible* diagrams. Or vice versa, the fully irreducible part Λ of the vertex is strongly localized in Matsubara space. Obviously we cannot conclude from this, that the fully irreducible vertex *is* the strongly localized part, because there is a variety of reducible diagrams that exhibit the full frequency dependence, i. e. decay in all directions. The first three diagrams in Fig. 2.3 are such reducible diagrams that vanish asymptotically, whereas the fourth diagram is an example of an irreducible fourth-order diagram.

2.2 Derivation

This section of my Thesis has been reused in Ref. [37].

In the following we derive the high-frequency asymptotics of the full two-particle vertex function F . Alternatively, and in a very similar manner, one may derive the asymptotical behavior of the two-particle Green's function or the generalized susceptibility. The former, however, is superior, because contrary to the susceptibility, the vertex can be parameterized very efficiently in its high-frequency region.

In order to describe this high-frequency asymptotics, we reiterate that outside of the low-frequency region only one contribution, the constant background, originates from the two-particle-irreducible vertex Λ . [36, 15] The remaining high-frequency-structures are contained in the vertices Φ^ℓ reducible in channel ℓ and can be parameterized through much simpler one- and two-frequency objects, coined Kernel-1 and Kernel-2 functions. [36, 15] The constant background can be identified as the bare vertex U_{abcd} shown in Fig. 2.4, which is the lowest-order term in the diagrammatic series for the full vertex.

Next, we have the Kernel-1 diagrams that only depend on one bosonic frequency and are depicted in Fig. 2.5. Here, two pairs of (incoming or outgoing) lines enter at the respective same interaction U . In this case the vertex depends only on the total transferred frequency at these interactions (it is the same bosonic frequency for both pairs because of energy conservation). [36, 15] There are three diagrams in Fig. 2.5 and hence there are three Kernel-1 contributions each of which depends on a single bosonic frequency. Switching from Matsubara frequencies to imaginary times, as defined in Eq. (1.17), it turns out that the dependence on frequency differences corresponds to diagrams with pairwise equal times. That is, the diagrams shown in Fig. 2.5 correspond to the summation of all terms with two equal-time pairs.

For the Kernel-2 diagrams of Fig. 2.6, we have only one pair of external legs that enter at the same U . Hence such diagrams depend on the transferred bosonic frequency at this U and (because of energy conservation) one additional fermionic frequency of the unpaired legs. This corresponds to one equal-time pair in Fourier space. All the diagrams Fig. 2.5 and Fig. 2.6 are two-particle reducible and thus, the asymptotic form of the full vertex F consists, apart from the constant background U , only of reducible terms Φ_{asympt}^ℓ .

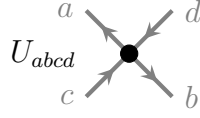


Figure 2.4: Diagram of the bare local interaction U . The bare vertex does not contain any Green's function, the (amputated) legs drawn in gray indicate the direction of the incoming/outgoing particles and their spin-orbital flavor a, b, c, d (the Matsubara frequencies are suppressed for simplicity).

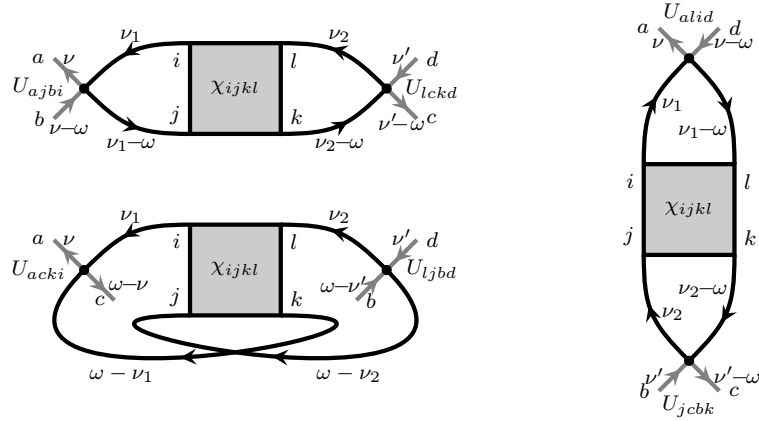


Figure 2.5: Vertex diagrams that depend on only one bosonic frequency, in ph -channel (top left), $\bar{p}\bar{h}$ -channel (right) and pp -channel (bottom left). Frequencies are given in the channel-specific notation (see Appendix A).

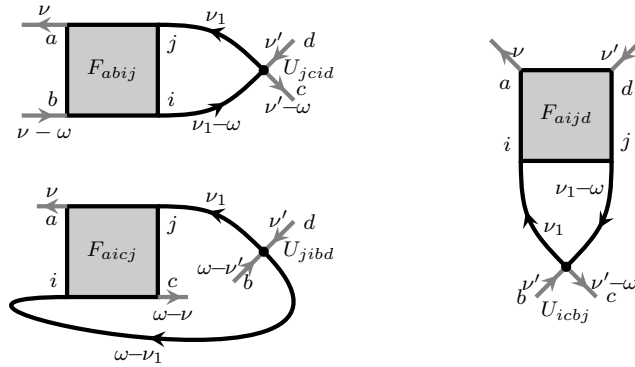


Figure 2.6: Vertex diagrams that depend on one bosonic and one fermionic frequency, in ph -channel (top left), $\bar{p}\bar{h}$ -channel (right) and pp -channel (bottom left). Frequencies are given in the channel-specific notation (see Appendix A).

2.2.1 Equal-time two-particle Green's functions

We now have to find a way to extract the aforementioned asymptotics from Green's function-like quantities, which are accessible in impurity solvers such as CT-QMC.

Considering the full Green's function $G_{ijkl}(\tau_1, \tau_2, \tau_3, \tau_4)$, we need to form two equal-time pairs for the diagrams of Fig. 2.5 to arrive at a function of two time arguments or one frequency-difference. There are three distinct ways to achieve this:

$$\tau_1 = \tau_2 \equiv \tau, \quad \tau_3 = \tau_4 \equiv \tau' \quad (2.5)$$

$$\tau_1 = \tau_3 \equiv \tau, \quad \tau_2 = \tau_4 \equiv \tau' \quad (2.6)$$

$$\tau_1 = \tau_4 \equiv \tau, \quad \tau_2 = \tau_3 \equiv \tau' \quad (2.7)$$

which relate to the ph , pp and $\overline{p\bar{h}}$ channel. The “two-legged” two-particle Green's function for the ph -channel, defined in (2.5), is

$$G_{ijkl}^{ph, \nu_1 - \nu_2} = \int d\tau d\tau' e^{i(\nu_1 - \nu_2)(\tau - \tau')} \langle T_\tau d_i(\tau) d_j^\dagger(\tau) d_k(\tau') d_l^\dagger(\tau') \rangle, \quad (2.8)$$

and for the pp -channel, we get

$$G_{ijkl}^{pp, \nu_1 + \nu_3} = \int d\tau d\tau' e^{i(\nu_1 + \nu_3)(\tau - \tau')} \langle T_\tau d_i(\tau) d_j^\dagger(\tau') d_k(\tau) d_l^\dagger(\tau') \rangle. \quad (2.9)$$

While the above functions have to be measured separately, the third, related to the $\overline{p\bar{h}}$ -channel, can be obtained from the first by the crossing relation (see Ref. [33] for an illustration)

$$G_{ijkl}^{\overline{p\bar{h}}} = -G_{ilkj}^{ph} \quad (2.10)$$

and depends on the frequency difference $\nu_1 - \nu_4$.

From the six ways to form one equal-time pair as needed for the diagrams Fig. 2.5, it is sufficient to consider only the following three, with the others related by time-reversal symmetry:

$$\tau_1 \equiv \tau, \quad \tau_2 \equiv \tau', \quad \tau_3 = \tau_4 \equiv \tau'', \quad (2.11)$$

$$\tau_1 \equiv \tau, \quad \tau_3 \equiv \tau', \quad \tau_2 = \tau_4 \equiv \tau'', \quad (2.12)$$

$$\tau_1 \equiv \tau, \quad \tau_4 \equiv \tau', \quad \tau_2 = \tau_3 \equiv \tau''. \quad (2.13)$$

Here, Eqs. (2.11)-(2.13) are related, as before, to the ph , pp and $\overline{p\bar{h}}$ channel. The “three-legged” two-particle Green’s function in the ph -channel corresponding to Eq. (2.11) follows as

$$G_{ijkl}^{ph, \nu_1, \nu_1 - \nu_2} = \int d\tau d\tau' d\tau'' e^{i(\nu_1(\tau - \tau') + (\nu_1 - \nu_2)(\tau' - \tau''))} \langle T_\tau d_i(\tau) d_j^\dagger(\tau') d_k(\tau'') d_l^\dagger(\tau'') \rangle, \quad (2.14)$$

and in the pp -channel (Eq. (2.12)) it is

$$G_{ijkl}^{pp, \nu_1, \nu_1 + \nu_3} = \int d\tau d\tau' d\tau'' e^{i(\nu_1(\tau - \tau') + (\nu_1 + \nu_3)(\tau' - \tau''))} \langle T_\tau d_i(\tau) d_j^\dagger(\tau'') d_k(\tau') d_l^\dagger(\tau'') \rangle. \quad (2.15)$$

Again, the Green’s function in the $\overline{p\bar{h}}$ -channel can be obtained by the crossing relation Eq. (2.10), the frequency arguments are then ν_1 and $\nu_1 - \nu_4$. Please note that $\nu_1 - \nu_2$, $\nu_1 + \nu_3$ and $\nu_1 - \nu_4$ are referred to as the channel-specific bosonic Matsubara frequencies ω_{ph} , ω_{pp} and $\omega_{\overline{p\bar{h}}}$, respectively. A full table with channel-specific frequency notations is given in Appendix A.

2.2.2 Subtraction of disconnected parts

We have seen in Eq. (1.60) and Eq. (1.61), that the full two-particle Green’s function, as measured in CT-QMC, contains one connected and also two disconnected parts. Hence, in order to arrive at the two- and three-legged diagrams of Fig. 2.5 and Fig. 2.6, it is necessary to eliminate the disconnected terms. In the following we will assume the one-particle Green’s function to be flavor diagonal, such that $G_{ij}(\tau_1, \tau_2) \equiv G_i(\tau_1, \tau_2) \delta_{ij}$. We recover the physical single-frequency susceptibility in the particle-hole channel by subtracting the constant “straight term”,

$$\chi_{ijkl}^{ph, \omega} = G_{ijkl}^{ph, \omega} - (1 - n_i)(1 - n_k) \delta_{\omega 0} \delta_{ij} \delta_{kl}, \quad (2.16)$$

whereas the particle-particle susceptibility is already given by

$$\chi_{ijkl}^{pp, \omega} = G_{ijkl}^{pp, \omega}. \quad (2.17)$$

We will now turn to the three-legged Green’s functions, where we are again interested only in the connected part corresponding to Fig. 2.6. For the particle-hole

channel we find

$$\chi_{ijkl}^{c,ph,\nu\omega} = G_{ijkl}^{ph,\nu\omega} - G_i^\nu \left[(n_k - 1) \delta_{ij} \delta_{kl} \delta_{\omega 0} - G_k^{\nu-\omega} \delta_{il} \delta_{jk} \right] \quad (2.18)$$

and for the particle-particle channel

$$\chi_{ijkl}^{c,pp,\nu\omega} = G_{ijkl}^{pp,\nu\omega} - (\delta_{ij} \delta_{kl} - \delta_{il} \delta_{jk}) G_i^\nu G_k^{\omega-\nu}. \quad (2.19)$$

As usual, the corresponding expressions for the transverse particle-hole channel can be obtained by applying the crossing relation Eq. (2.10).

2.2.3 Kernel functions

After the subtraction of the disconnected parts from the two-particle Green functions, the next step is to contract the equal-time legs with interaction vertices. The two-legged objects have two pairs of equal times and therefore need two distinct bare vertices to contract their legs and obtain the Kernel-1 functions $K^{(1),\ell}$:

$$K_{abcd}^{(1),ph,\omega} = - \sum_{ijkl} U_{ajbi} \chi_{ijkl}^{ph,\omega} U_{lckd} \quad (2.20)$$

$$K_{abcd}^{(1),\bar{p}h,\omega} = - \sum_{ijkl} U_{alid} \chi_{ijkl}^{\bar{p}h,\omega} U_{jcbk} \quad (2.21)$$

$$K_{abcd}^{(1),pp,\omega} = - \sum_{ijkl} \frac{U_{acki}}{2} \chi_{ijkl}^{pp,\omega} \frac{U_{ljb d}}{2} \quad (2.22)$$

This corresponds precisely to the diagrams shown in Fig. 2.5.

For the Kernel-2 approximations, the procedure is a bit more involved. After the bare vertex contraction, we need to amputate the remaining legs. Thus, the Kernel-2 functions $K^{(2),\ell}$ in all three channels are

$$K_{abcd}^{(2),ph,\nu\omega} = \sum_{ij} \frac{-\chi_{abji}^{c,ph,\omega}}{G_a^\nu G_b^{\nu-\omega}} U_{icjd} - K_{abcd}^{(1),ph,\omega} \quad (2.23)$$

$$K_{abcd}^{(2),\bar{p}h,\nu\omega} = \sum_{ij} \frac{-\chi_{aijd}^{c,\bar{p}h,\omega}}{G_a^\nu G_d^{\nu-\omega}} U_{icbj} - K_{abcd}^{(1),\bar{p}h,\omega} \quad (2.24)$$

$$K_{abcd}^{(2),pp,\nu\omega} = \sum_{ij} \frac{-\chi_{aicj}^{c,pp,\omega}}{G_a^\nu G_c^{\nu-\omega}} \frac{U_{jib d}}{2} - K_{abcd}^{(1),pp,\omega}, \quad (2.25)$$

where we had to subtract the Kernel-1 functions in order to avoid double-counting of diagrams.

Now we have six functions going to zero for high frequencies ν or ω , from which we can compile the asymptotic vertex.

2.2.4 Asymptotic form of the full vertex

According to the (local) parquet equation, the full vertex F_{abcd} can be decomposed into a fully irreducible and several reducible parts:

$$F_{abcd}^{\nu\nu'\omega} = \Lambda_{abcd}^{\nu\nu'\omega} + \Phi_{abcd}^{ph,\nu\nu'\omega} + \Phi_{abcd}^{\overline{ph},\nu\nu'\omega} + \Phi_{abcd}^{pp,\nu\nu'\omega}. \quad (2.26)$$

We are now able to construct the asymptotic form of the reducible vertices Φ [36] using:

$$\Phi_{abcd}^{\text{asympt},\ell,\nu\nu'\omega} = K_{abcd}^{(1),\ell,\omega} + K_{abcd}^{(2),\ell,\nu\omega} + \overline{K}_{abcd}^{(2),\ell,\nu'\omega}, \quad (2.27)$$

where the functions $\overline{K}^{(2),\ell}$ are found to be equal to $K^{(2),\ell}$ due to time-reversal symmetry. Therefore summing up all $K^{(i),\ell}$, we get the asymptotic form of the full vertex:

$$\begin{aligned} F_{abcd}^{\text{asympt}}(\nu_\ell, \nu'_\ell, \omega_\ell) - U_{abcd} &= K_{abcd}^{(1),ph,\omega_{ph}} + K_{abcd}^{(2),ph,\nu_{ph}\omega_{ph}} + K_{abcd}^{(2),ph,\nu'_{ph}\omega_{ph}} \\ &\quad + K_{abcd}^{(1),\overline{ph},\omega_{\overline{ph}}} + K_{abcd}^{(2),\overline{ph},\nu_{\overline{ph}}\omega_{\overline{ph}}} + K_{abcd}^{(2),\overline{ph},\nu'_{\overline{ph}}\omega_{\overline{ph}}} \\ &\quad + K_{abcd}^{(1),pp,\omega_{pp}} + K_{abcd}^{(2),pp,\nu_{pp}\omega_{pp}} + K_{abcd}^{(2),pp,\nu'_{pp}\omega_{pp}} \end{aligned} \quad (2.28)$$

In this way we are now able to build arbitrarily large vertices in any frequency notation, which leads to significant improvements of further calculations.

2.3 Analytical calculations for the atomic limit

For testing, it is very useful to have the possibility to compare results with analytical calculations. A general analytic solution of the Hubbard model or the Anderson impurity model has not been found yet, but there is a limiting case that is very well tractable in formulas. It is the limit of no hopping, also coined *atomic limit*.

The Hamiltonian of the atomic limit for the one-band case,

$$H = -\mu(n_{\uparrow} + n_{\downarrow}) + Un_{\uparrow}n_{\downarrow}, \quad (2.29)$$

is obtained by setting the hopping or hybridization to zero. The Lehmann basis for this model

$$\{|0\rangle, |\uparrow\rangle, |\downarrow\rangle, |\uparrow\downarrow\rangle\} \quad (2.30)$$

is also an eigenbasis of the Hamiltonian (2.29). This greatly simplifies the calculation of expectation values. The annihilation operators and the Hamiltonian in this basis are

$$c_{\uparrow} = \begin{pmatrix} 0 & 1 & 0 & 0 \\ 0 & 0 & 0 & 0 \\ 0 & 0 & 0 & 1 \\ 0 & 0 & 0 & 0 \end{pmatrix}, \quad c_{\downarrow} = \begin{pmatrix} 0 & 0 & 1 & 0 \\ 0 & 0 & 0 & -1 \\ 0 & 0 & 0 & 0 \\ 0 & 0 & 0 & 0 \end{pmatrix}, \quad H = \begin{pmatrix} 0 & 0 & 0 & 0 \\ 0 & -\mu & 0 & 0 \\ 0 & 0 & -\mu & 0 \\ 0 & 0 & 0 & U - 2\mu \end{pmatrix}. \quad (2.31)$$

For the case $U = 2\mu$, the number of distinct eigen-energies is reduced to two, and calculations become even simpler. Let us first evaluate the expectation value of the occupation operator $n_{\uparrow} = c_{\uparrow}^{\dagger}c_{\uparrow}$ with the Lehmann representation $n_{\uparrow} = \text{diag}(0, 1, 0, 1)$. Due to SU(2) symmetry, the expectation value of n_{\downarrow} is the same.

$$\langle \hat{n}_{\uparrow} \rangle = \frac{\text{Tr} [e^{-\beta H} c_{\uparrow}^{\dagger} c_{\uparrow}]}{\text{Tr} [e^{-\beta H}]} = \frac{1 + e^{\beta\mu}}{2(1 + e^{\beta\mu})} = \frac{1}{2} \quad (2.32)$$

This means, that the condition $\mu = U/2$ generates a half-filled system.

Next, we calculate the interacting one-particle Greens-function, where we omit the spin index, because G_{\uparrow} and G_{\downarrow} are identical:

$$G(\tau) = -\frac{\text{Tr} [e^{-\beta H} c(\tau) c^{\dagger}]}{\text{Tr} [e^{-\beta H}]} = -\frac{e^{U\tau/2} + e^{(\beta-\tau)U/2}}{2(1 + e^{\beta U/2})}, \quad (2.33)$$

where τ was chosen larger than zero to fulfil the time-ordering. In fermionic Matsubara frequencies $i\nu$ this corresponds to

$$G^{\nu} = \int_0^{\beta} d\tau e^{i\nu\tau} G(\tau) = \frac{1}{i\nu - \frac{U^2}{4i\nu}} = -\frac{i\nu}{\nu^2 + \frac{U^2}{4}}, \quad (2.34)$$

i. e. $\Sigma^\nu = U^2/(4i\nu)$. The calculation of the two-particle Green's function and subsequently the vertex F can be done in the same way [14, 15]. But since it is rather lengthy, we just give the result here (in the form used in [36] with frequencies adapted to our convention).

$$F_{\uparrow\downarrow} = \mathcal{F}_{odd} + \mathcal{F}_{pp} + \mathcal{F}_{ph} + \mathcal{F}_{\overline{ph}} \quad (2.35)$$

with

$$\mathcal{F}_{odd} = U - \frac{U^3 \sum \nu_i^2}{8 \prod \nu_i} - \frac{3U^5}{16} \prod \frac{1}{\nu_i}, \quad (2.36)$$

$$\mathcal{F}_{pp} = -\frac{\beta U^2}{2} f\left(\frac{U}{2}\right) D^{\nu_{pp}\nu'_{pp}} \delta_{\omega_{pp},0}, \quad (2.37)$$

$$\mathcal{F}_{ph} = -\frac{\beta U^2}{4} \left(f\left(\frac{U}{2}\right) - f\left(-\frac{U}{2}\right) \right) D^{\nu_{ph}\nu'_{ph}} \delta_{\omega_{ph},0}, \quad (2.38)$$

$$\mathcal{F}_{\overline{ph}} = \frac{\beta U^2}{2} f\left(-\frac{U}{2}\right) D^{\nu_{\overline{ph}}\nu'_{\overline{ph}}} \delta_{\omega_{\overline{ph}},0}, \quad (2.39)$$

$$F_{\uparrow\uparrow} = \frac{\beta U^2}{4} \left(D^{\nu_{\overline{ph}}\nu'_{\overline{ph}}} \delta_{\omega_{\overline{ph}},0} - D^{\nu_{ph}\nu'_{ph}} \delta_{\omega_{ph},0} \right) = \frac{\beta U^2}{4} D^{\nu_1\nu_3} (\delta_{\nu_1\nu_4} - \delta_{\nu_1\nu_2}), \quad (2.40)$$

$$F_{\uparrow\downarrow}^{\nu\nu'\omega} = -F_{\uparrow\downarrow}^{\nu(\nu-\omega)(\nu-\nu')}. \quad (2.41)$$

Here, $f(\varepsilon) = 1/(1 + e^{\beta\varepsilon})$ is the Fermi function and the abbreviation $D^{\nu\nu'}$ stands for

$$D^{\nu\nu'} = \frac{1}{\nu^2\nu'^2} \left(\nu^2 + \frac{U^2}{4} \right) \left(\nu'^2 + \frac{U^2}{4} \right). \quad (2.42)$$

From these results, we can later on derive the asymptotic form of the vertex (as done already in Ref. [36]) to verify our approach.

Let us now imitate the process described in Sec. 2.2. First, we need to calculate the equal-time Green's functions by the formulas given there. In the atomic limit, the expectation values can be computed by taking the traces in the Lehmann basis. The half-filling results for the ‘‘two-legged’’ Green's functions $P_{abcd}^{(2),\ell,\omega} \equiv G_{abcd}^{(\ell),\omega}$ are given in Table 2.1 and for the ‘‘three-legged’’ $P_{abcd}^{(3),\ell,\nu\omega} \equiv G_{abcd}^{(\ell),\nu\omega}$ in Table 2.2.

$P^{(2),\ell,\omega}$	pp	ph
$\uparrow\uparrow$	0	$\frac{\beta}{2}\delta_{\omega 0}$
$\uparrow\downarrow$	$\frac{\beta}{2}f\left(\frac{U}{2}\right)\delta_{\omega 0}$	$\frac{\beta}{2}f\left(\frac{U}{2}\right)\delta_{\omega 0}$
$\overline{\uparrow\downarrow}$	$-\frac{\beta}{2}f\left(\frac{U}{2}\right)\delta_{\omega 0}$	$\frac{\beta}{2}f\left(-\frac{U}{2}\right)\delta_{\omega 0}$

Table 2.1: Two-legged Green's functions $P^{(2)}$ in particle-particle and longitudinal particle-hole channel. Frequencies are given in the channel-specific notations, see Appendix A.

$P^{(3),\ell,\nu\omega}$	pp	ph
$\uparrow\uparrow$	0	$\frac{\nu(\nu-\omega)-\frac{U^2}{4}}{\left(\nu^2+\frac{U^2}{4}\right)\left((\nu-\omega)^2+\frac{U^2}{4}\right)} + \delta_{\omega 0}\frac{\beta}{2}\frac{\frac{U}{2}\tanh\frac{\beta U}{4}+i\nu}{\nu^2+\frac{U^2}{4}}$
$\uparrow\downarrow$	$\frac{\nu(\nu-\omega)-\frac{U^2}{4}}{\left(\nu^2+\frac{U^2}{4}\right)\left((\nu-\omega)^2+\frac{U^2}{4}\right)} - \delta_{\omega 0}\frac{\beta\frac{U}{2}f\left(\frac{U}{2}\right)}{\nu^2+\frac{U^2}{4}}$	$\delta_{\omega 0}\frac{\beta}{2}\frac{-\frac{U}{2}+i\nu}{\nu^2+\frac{U^2}{4}}$
$\overline{\uparrow\downarrow}$	$-\frac{\nu(\nu-\omega)-\frac{U^2}{4}}{\left(\nu^2+\frac{U^2}{4}\right)\left((\nu-\omega)^2+\frac{U^2}{4}\right)} + \delta_{\omega 0}\frac{\beta\frac{U}{2}f\left(\frac{U}{2}\right)}{\nu^2+\frac{U^2}{4}}$	$\frac{\nu(\nu-\omega)-\frac{U^2}{4}}{\left(\nu^2+\frac{U^2}{4}\right)\left((\nu-\omega)^2+\frac{U^2}{4}\right)} + \delta_{\omega 0}\frac{\beta\frac{U}{2}f\left(-\frac{U}{2}\right)}{\nu^2+\frac{U^2}{4}}$

Table 2.2: Three-legged Green's functions $P^{(3)}$ in particle-particle and longitudinal particle-hole channel. Frequencies are given in the channel-specific notations, see Appendix A.

2.3.1 From $P^{(2)}$ to $K^{(1)}$

Disconnected parts

The $K^{(1)}$ functions are then obtained from the susceptibility, which is in turn obtained from the $P^{(2)}$ function by subtracting all constant terms, according to Eqs. (2.16) and (2.17). In the atomic limit at half filling, the constant term of Eq. (2.16) is $\frac{1}{4}\beta\delta_{\omega_0}$. The modifications are then

$$\chi_{\uparrow\uparrow}^{ph,\omega} = \frac{1}{2}\beta\delta_{\omega_0} - \frac{1}{4}\beta\delta_{\omega_0} = \frac{1}{4}\beta\delta_{\omega_0} \quad (2.43)$$

$$\chi_{\uparrow\downarrow}^{ph,\omega} = \frac{\beta}{2}f\left(\frac{U}{2}\right)\delta_{\omega_0} - \frac{1}{4}\beta\delta_{\omega_0} = -\frac{1}{4}\beta\delta_{\omega_0}\left(f\left(-\frac{U}{2}\right) - f\left(\frac{U}{2}\right)\right), \quad (2.44)$$

in the other cases, the susceptibilities are identical to the one-frequency Green's functions $P^{(2)}$.

U-matrix multiplication

To get the kernel functions $K^{(1)}$ from the susceptibilities, we have to invert their sign, because the vertex F is defined with a sign relative to the connected susceptibility. The one-band U-matrix has only four non-vanishing elements:

$$U_{\uparrow\downarrow\uparrow\downarrow} = U_{\downarrow\uparrow\downarrow\uparrow} = U \quad (2.45)$$

$$U_{\uparrow\uparrow\uparrow\uparrow} = U_{\downarrow\downarrow\downarrow\downarrow} = -U \quad (2.46)$$

In the particle-hole channel, the U-matrix multiplication in Eq. (2.20) takes the following simple form,

$$K_{\uparrow\uparrow}^{(1),ph,\omega} = -U_{\uparrow\downarrow\uparrow\downarrow}\chi_{\downarrow\downarrow}^{ph,\omega}U_{\downarrow\uparrow\downarrow\uparrow} \stackrel{\text{SU}(2)}{=} -U^2\chi_{\uparrow\uparrow}^{ph,\omega} \quad (2.47)$$

$$K_{\uparrow\downarrow}^{(1),ph,\omega} = -U_{\uparrow\downarrow\uparrow\downarrow}\chi_{\downarrow\uparrow}^{ph,\omega}U_{\uparrow\downarrow\uparrow\downarrow} \stackrel{\text{SU}(2)}{=} -U^2\chi_{\uparrow\downarrow}^{ph,\omega} \quad (2.48)$$

$$K_{\downarrow\downarrow}^{(1),ph,\omega} = -U_{\uparrow\downarrow\uparrow\downarrow}\chi_{\uparrow\downarrow}^{ph,\omega}U_{\uparrow\downarrow\uparrow\downarrow} \stackrel{\text{SU}(2)}{=} -U^2\chi_{\downarrow\downarrow}^{ph,\omega}, \quad (2.49)$$

where the double matrix multiplication is effectively reduced to an ordinary multiplication by U^2 . In the particle-particle channel on the other hand, the matrix

$K^{(1),\ell,\omega}$	pp	ph
$\uparrow\uparrow$	0	$-\frac{\beta U^2}{4} \delta_{\omega 0}$
$\uparrow\downarrow$	$-\frac{\beta U^2}{2} f\left(\frac{U}{2}\right) \delta_{\omega 0}$	$\frac{\beta U^2}{4} \left[f\left(-\frac{U}{2}\right) - f\left(\frac{U}{2}\right) \right] \delta_{\omega 0}$
$\uparrow\bar{\downarrow}$	$\frac{\beta U^2}{2} f\left(\frac{U}{2}\right) \delta_{\omega 0}$	$-\frac{\beta U^2}{2} f\left(-\frac{U}{2}\right) \delta_{\omega 0}$

Table 2.3: Kernel functions $K^{(1)}$ in particle-particle and longitudinal particle-hole channel. Frequencies are given in the channel-specific notations.

multiplication involves all non-vanishing terms:

$$K_{\uparrow\downarrow}^{(1),pp,\omega} = -\frac{1}{4} \left[U_{\uparrow\downarrow\uparrow\downarrow} \chi_{\downarrow\uparrow}^{pp,\omega} U_{\uparrow\downarrow\uparrow\downarrow} + U_{\uparrow\downarrow\uparrow\downarrow} \chi_{\uparrow\downarrow}^{pp,\omega} U_{\uparrow\downarrow\uparrow\downarrow} \right. \\ \left. + U_{\uparrow\downarrow\uparrow\downarrow} \chi_{\uparrow\bar{\downarrow}}^{pp,\omega} U_{\uparrow\downarrow\uparrow\downarrow} + U_{\uparrow\downarrow\uparrow\downarrow} \chi_{\uparrow\bar{\downarrow}}^{pp,\omega} U_{\uparrow\downarrow\uparrow\downarrow} \right] \stackrel{\text{CS, SU}(2)}{=} -U^2 \chi_{\uparrow\downarrow} \quad (2.50)$$

$$K_{\uparrow\bar{\downarrow}}^{(1),pp,\omega} = -\frac{1}{4} \left[U_{\uparrow\downarrow\uparrow\downarrow} \chi_{\downarrow\uparrow}^{pp,\omega} U_{\uparrow\downarrow\uparrow\downarrow} + U_{\uparrow\downarrow\uparrow\downarrow} \chi_{\uparrow\downarrow}^{pp,\omega} U_{\uparrow\downarrow\uparrow\downarrow} \right. \\ \left. + U_{\uparrow\downarrow\uparrow\downarrow} \chi_{\downarrow\uparrow}^{pp,\omega} U_{\uparrow\downarrow\uparrow\downarrow} + U_{\uparrow\downarrow\uparrow\downarrow} \chi_{\uparrow\downarrow}^{pp,\omega} U_{\uparrow\downarrow\uparrow\downarrow} \right] \stackrel{\text{CS, SU}(2)}{=} -U^2 \chi_{\uparrow\bar{\downarrow}} \quad (2.51)$$

Due to SU(2) and crossing symmetry (CS), also here a simple multiplication can be applied, but it serves as an explanation, why it is necessary to associate a factor $\frac{1}{2}$ with every U-matrix in the particle-particle channel. All $K^{(1)}$ functions are given in Table 2.3.

2.3.2 From $P^{(3)}$ to $K^{(2)}$

Disconnected parts subtraction and amputation of external legs

In order to calculate the $K^{(2)}$ functions, we need to subtract all disconnected diagrams from the $P^{(3)}$ functions, as specified in Eqs. (2.18) and (2.19), and then amputate the remaining legs. For this purpose, it is of advantage to rewrite the

$P^{(3)}$ functions of Table 2.2 in terms of Green's and $K^{(1)}$ -functions.

$$P_{\uparrow\uparrow}^{(3),ph,\nu\omega} = -\frac{1}{2}\beta\delta_{\omega 0}G^\nu - G^\nu G^{\nu-\omega} + \underbrace{\left[\frac{U^2}{4\nu(\nu-\omega)} - \frac{K_{\uparrow\downarrow}^{(1),ph,\omega}}{U} \left(1 + \frac{U^2}{4\nu^2}\right) \right]}_{-L_{\uparrow\uparrow}^{ph,\nu\omega}} G^\nu G^{\nu-\omega} \quad (2.52)$$

$$P_{\uparrow\downarrow}^{(3),ph,\nu\omega} = -\frac{1}{2}\beta\delta_{\omega 0}G^\nu + \underbrace{\left[-\frac{K_{\uparrow\uparrow}^{(1),ph,\omega}}{U} \left(1 + \frac{U^2}{4\nu^2}\right) \right]}_{-L_{\uparrow\downarrow}^{ph,\nu\omega}} G^\nu G^{\nu-\omega} \quad (2.53)$$

$$P_{\downarrow\downarrow}^{(3),ph,\nu\omega} = -G^\nu G^{\nu-\omega} + \underbrace{\left[\frac{U^2}{4\nu(\nu-\omega)} + \frac{K_{\uparrow\downarrow}^{(1),ph,\omega}}{U} \left(1 + \frac{U^2}{4\nu^2}\right) \right]}_{-L_{\downarrow\downarrow}^{ph,\nu\omega}} G^\nu G^{\nu-\omega} \quad (2.54)$$

In the particle-particle channel it is sufficient to print the $\uparrow\downarrow$ -component, because the $\uparrow\downarrow$ -component differs only by a sign and the $\uparrow\uparrow$ -component vanishes.

$$P_{\uparrow\downarrow}^{(3),pp,\nu\omega} = G^\nu G^{\omega-\nu} + \underbrace{\left[\frac{U^2}{4\nu(\omega-\nu)} + \frac{K_{\uparrow\downarrow}^{(1),pp,\omega}}{U} \left(1 + \frac{U^2}{4\nu^2}\right) \right]}_{-L_{\uparrow\downarrow}^{pp,\nu\omega}} G^\nu G^{\omega-\nu} \quad (2.55)$$

Note, that also here the kernel part L has a negative sign, for the same reason as mentioned above. The disconnected terms are written in green, the legs in brown color and we see that they are indeed in accordance with Eqs. (2.18) and (2.19).

U-matrix multiplication

In the previous paragraph we showed how to extract the kernel part L from the two-frequency Green's functions $P^{(3)}$. The next step is the multiplication with the

$K^{(2),\ell,\nu\omega}$	pp	ph
$\uparrow\uparrow$	0	$K_{\uparrow\uparrow}^{(1),ph,\omega} \frac{U^2}{4\nu^2}$
$\uparrow\downarrow$	$\frac{U^2}{4\nu(\nu-\omega)}(K_{\uparrow\downarrow}^{(1),pp,\omega} - U)$	$\frac{U^2}{4\nu(\nu-\omega)}(K_{\uparrow\downarrow}^{(1),ph,\omega} - U)$
$\uparrow\downarrow$	$-\frac{U^2}{4\nu(\nu-\omega)}(K_{\uparrow\downarrow}^{(1),pp,\omega} - U)$	$\frac{U^2}{4\nu(\nu-\omega)}(K_{\uparrow\downarrow}^{(1),ph,\omega} + U)$

Table 2.4: Kernel functions $K^{(2)}$ in particle-particle and longitudinal particle-hole channel. Frequencies are given in the channel-specific notations.

U-matrix, leading to the sum of $K^{(1)}$ and $K^{(2)}$ in each channel.

$$K_{\uparrow\uparrow}^{(1),ph,\omega} + K_{\uparrow\uparrow}^{(2),ph,\nu\omega} = U_{\uparrow\downarrow\uparrow\downarrow} L_{\downarrow\uparrow}^{ph,\nu\omega} = U L_{\uparrow\downarrow}^{ph,\nu\omega} \quad (2.56)$$

$$K_{\uparrow\downarrow}^{(1),ph,\omega} + K_{\uparrow\downarrow}^{(2),ph,\nu\omega} = U_{\uparrow\downarrow\uparrow\downarrow} L_{\downarrow\downarrow}^{ph,\nu\omega} = U L_{\uparrow\uparrow}^{ph,\nu\omega} \quad (2.57)$$

$$K_{\uparrow\downarrow}^{(1),ph,\omega} + K_{\uparrow\downarrow}^{(2),ph,\nu\omega} = U_{\uparrow\downarrow\uparrow\downarrow} L_{\uparrow\downarrow}^{ph,\nu\omega} = -U L_{\uparrow\downarrow}^{ph,\nu\omega} \quad (2.58)$$

$$K_{\uparrow\downarrow}^{(1),pp,\omega} + K_{\uparrow\downarrow}^{(2),pp,\nu\omega} = \frac{1}{2} [U_{\uparrow\downarrow\uparrow\downarrow} L_{\uparrow\downarrow}^{pp,\nu\omega} + U_{\uparrow\downarrow\uparrow\downarrow} L_{\downarrow\uparrow}^{pp,\nu\omega}] = -U L_{\uparrow\downarrow}^{pp,\nu\omega} \quad (2.59)$$

The equations above already allow for identifying the $K^{(2)}$ functions, they are printed in Table 2.4. Some $K^{(2)}$ -functions together with the corresponding $P^{(3)}$ -functions are drawn in Fig. 2.7. It is worth noting that all $K^{(1)}$ functions are proportional to δ_{ω_0} at half filling, a fact that has been exploited several times in the calculations leading to the results for $K^{(2)}$.

The kernel functions in the transversal particle-hole channel can be obtained from the longitudinal particle-hole channel due to crossing symmetry.

Kernel functions as high-frequency limits

In Ref. [36] the kernel functions of the atomic limit were obtained by taking the high-frequency limit of the vertex F . This approach is complementary to ours, therefore I will only give a short outline. Starting from F , the $K^{(1),\ell}$ functions are calculated by taking the limits in both fermionic frequencies:

$$K_{\sigma\sigma'}^{(1),\ell,\omega\ell} = \lim_{|\nu_\ell| \rightarrow \infty} \lim_{|\nu'_\ell| \rightarrow \infty} F_{\sigma\sigma'}^{\nu_1\nu_2\nu_3\nu_4} - (1 - \delta_{\sigma\sigma'}) \quad (2.60)$$

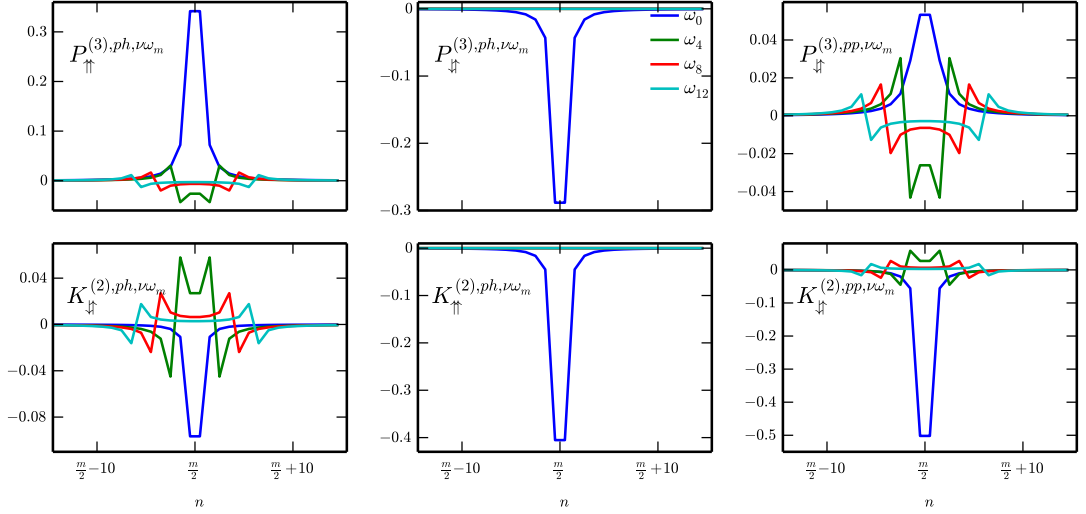


Figure 2.7: Upper row: Three-time Green's functions $P^{(3)}$, lower row: kernel functions $K^{(2)}$. Both are drawn as functions of the fermionic frequency $\nu = (2n + 1)\pi/\beta$ at four selected bosonic frequencies $\omega_m = 2m\pi/\beta$. The parameters are $U = 1$ and $\beta = 4$.

The $K^{(2)}$ functions result from one-frequency limits:

$$K_{\sigma\sigma'}^{(2),\ell,\nu_\ell\omega_\ell} = \lim_{|\nu'_\ell| \rightarrow \infty} F_{\sigma\sigma'}^{\nu_1\nu_2\nu_3\nu_4} - (1 - \delta_{\sigma\sigma'}) - K_{\sigma\sigma'}^{(1),\ell,\omega_\ell}, \quad (2.61)$$

where ℓ is one of $\{ph, \bar{p}\bar{h}, pp\}$ and the channel-specific frequencies ν_ℓ are given in Appendix A. The kernel functions extracted from Eqs. (2.35) and (2.35) with this approach are identical to the ones given in Tables 2.3 and 2.4.

2.3.3 The rest function

Having the kernel functions at our disposal, we may now assemble the asymptotic form of the full vertex by Eq. (2.28), see Fig. 2.8. It is, however, more interesting to calculate the difference R to the exact forms given in Eqs. (2.35), (2.40), and (2.41).

$$R_{\uparrow\downarrow}^{\nu_1\nu_2\nu_3\nu_4} = \frac{1}{\nu_1\nu_2\nu_3\nu_4} \left[r_0(U) + r_{ph}(\beta, U, \nu_1 - \nu_2) + r_{\bar{p}\bar{h}}(\beta, U, \nu_1 - \nu_4) + r_{pp}(\beta, U, \nu_1 + \nu_3) \right] \quad (2.62)$$

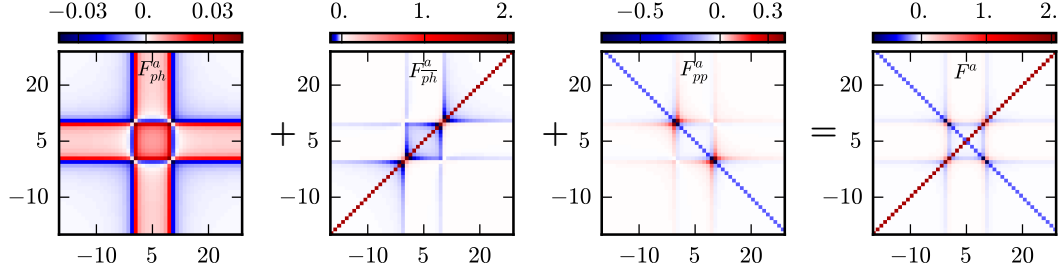


Figure 2.8: The ph -, \bar{ph} -, and pp -parts of the asymptotic vertex $F_{\uparrow\downarrow}^a - U$ (first three pictures) are defined by the first, second, and third line of the right-hand side of Eq. (2.28). The rightmost picture shows their sum $F_{\uparrow\downarrow}^a - U$. All slices are taken at ω_{10} in ph -notation. The parameters $U = 1$ and $\beta = 4$ are set to low values, such that also the structure of the pp -part becomes visible.

$$R_{\uparrow\uparrow}^{\nu_1\nu_2\nu_3\nu_4} = \frac{\beta U^6}{64} \frac{\delta_{\nu_1\nu_4} - \delta_{\nu_1, -\nu_3}}{\nu_1\nu_2\nu_3\nu_4} \quad (2.63)$$

$$R_{\uparrow\downarrow}^{\nu_1\nu_2\nu_3\nu_4} = -R_{\uparrow\downarrow}^{\nu_1\nu_4\nu_3\nu_2} \quad (2.64)$$

The functions r_ℓ , shown in Fig. 2.9, are given by

$$r_0(U) = -\frac{3U^5}{16} \quad (2.65)$$

$$r_{ph}(\beta, U, \omega) = \frac{\beta U^6}{64} \left(f\left(-\frac{U}{2}\right) - f\left(\frac{U}{2}\right) \right) \delta_{\omega 0} \quad (2.66)$$

$$r_{\bar{ph}}(\beta, U, \omega) = \frac{\beta U^6}{32} \left(-\frac{U}{2}\right) \delta_{\omega 0} \quad (2.67)$$

$$r_{pp}(\beta, U, \omega) = -\frac{\beta U^6}{32} 2f\left(\frac{U}{2}\right) \delta_{\omega 0} \quad (2.68)$$

These results show, that the asymptotic treatment is indeed correct, as the difference to the exact vertex is proportional to $\frac{1}{\nu_1\nu_2\nu_3\nu_4}$ (see left panel of Fig. 2.9) and hence decays in all frequency-directions, which was our initial requirement. Furthermore, at least in this special case, the asymptotic vertex captures all terms up to the order of U^4 .

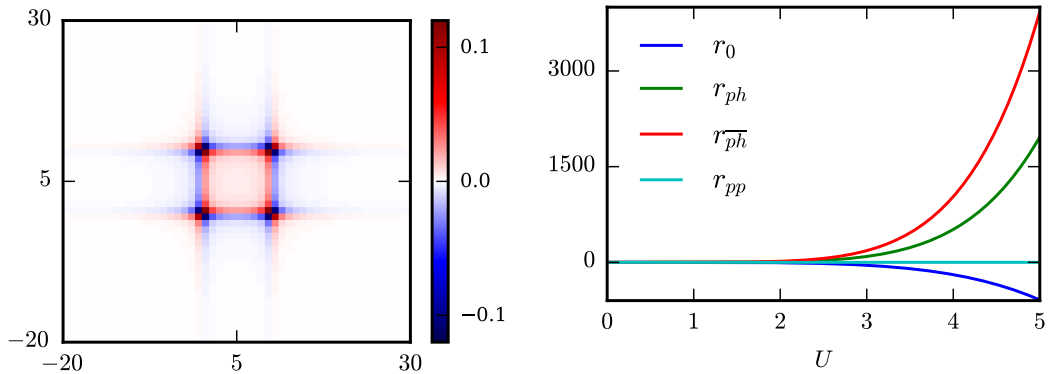


Figure 2.9: Left: The four-frequency decay $1/(\nu_1\nu_2\nu_3\nu_4)$, that is exhibited by R as a prefactor, in ph notation at $\omega_{ph} = 10$. Right: The functions $r_0(U)$, $r_{ph}(U)$, $r_{\overline{ph}}(U)$ and $r_{pp}(U)$, by which the prefactor is multiplied, at $\beta = 8$.

It is interesting and important to investigate the behaviour of the rest functions for different values of U and β . Already for intermediate values, such as $\beta = 8$ and $U = 2$, the Fermi functions $f(U/2)$ and $f(-U/2)$ are practically 0 and 1, respectively. Thus, we have approximately

$$r_{ph}(\beta, U, \omega) \approx \frac{\beta U^6}{64} \delta_{\omega 0}, \quad (2.69)$$

$$r_{\overline{ph}}(\beta, U, \omega) \approx \frac{\beta U^6}{32} \delta_{\omega 0}, \quad (2.70)$$

$$r_{pp}(\beta, U, \omega) \approx 0. \quad (2.71)$$

Clearly, the \overline{ph} -part is dominating, whereas the ph -part is half as large and the pp -part vanishes. The ratio of r_{ph} and the remaining r_0 is $-\beta U/4$, and thus they are of the same order of magnitude for intermediate U and β .

From a practical point of view, we note that the increase of the rest functions with U (and to a minor extent with β) means that the border of validity of the asymptotic vertex is shifted to higher frequencies as coupling strength increases (and temperature decreases).

Chapter 3

Applications and results

In this chapter, some results of applying the asymptotics in actual calculations will be shown. Partly they have been reused in Ref. [37].

3.1 ED-benchmark: 3D one-band Hubbard model

Exact diagonalization (ED) is a method that can solve the Anderson impurity problem exactly for a given discretized bath. The QMC solver of `w2DYNAMICS` is executed for the same bath and hybridization parameters that describe the impurity problem that is obtained in ED for the Hubbard model at convergence of the DMFT equations. Up to stochastic noise, the QMC solution then agrees with ED, which makes it a valuable benchmark.

In the following, all energies are in units of half the standard deviation of the non-interacting density of states $D = 2\sqrt{6}t \equiv 1$.

3.1.1 High-frequency cutoff of kernel functions

Fig. 3.1 shows some components of the two-time Green's function $P^{(2)}$ along with the corresponding $K^{(1)}$ kernel functions. The values are comparable to the results for the atomic limit in the ph channel, and at least qualitatively similar in the pp -channel. In Fig. 3.2, slices through $P^{(3)}$ and $K^{(2)}$ function at certain values of the bosonic frequency ω are drawn. The $\uparrow\uparrow$ and $\uparrow\downarrow$ components are swapped in the second row, because due to the U -matrix multiplication $K_{\uparrow\uparrow}^{(2)}$ and $K_{\uparrow\downarrow}^{(2)}$ are related to $P_{\uparrow\downarrow}^{(3)}$ and $P_{\uparrow\uparrow}^{(3)}$, respectively. Also here, some qualitative similarity to the atomic

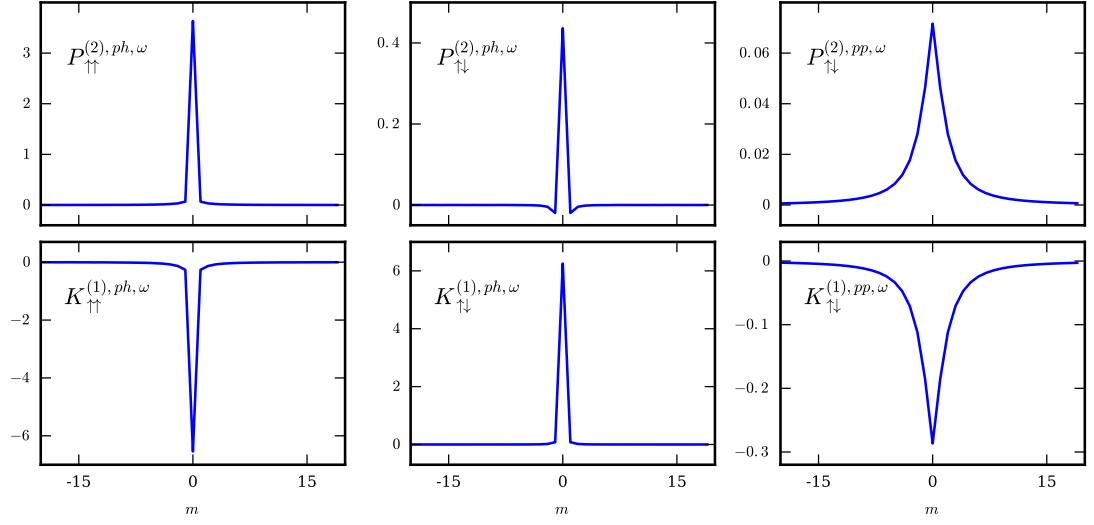


Figure 3.1: Upper row: two-time Green's functions $P^{(2)}$. Lower row: kernel functions $K^{(1)}$ for the 3D Hubbard model at $U=2D$, $\beta=8/D$. Both are drawn on the same axis of bosonic Matsubara frequencies $\omega_n = 2\pi n/\beta$. Notice the similarity of the particle-hole channel to the functions for the atomic limit in Tables 2.1 and 2.3.

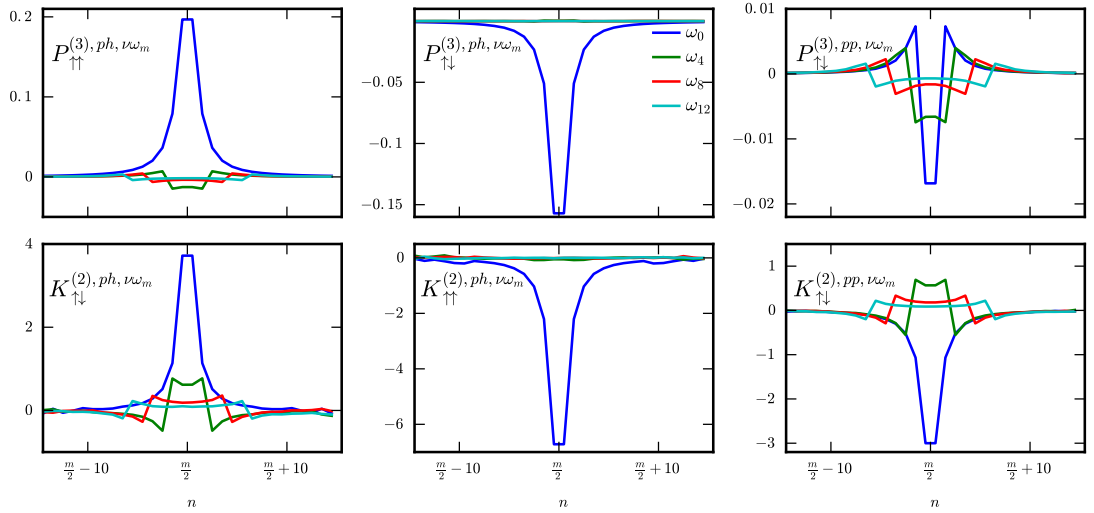


Figure 3.2: Upper row: two-time Green's functions P_3 , lower row: kernel functions K_2 for the 3D Hubbard model at $U=2D$, $\beta=8/D$. Both are drawn on the same axis of fermionic Matsubara frequencies. Notice the similarity of some components to the functions for the atomic limit in Fig. 2.7.

limit (Fig. 2.7) can be observed.

At higher values of the frequency arguments, both the $K^{(1)}$ and $K^{(2)}$ functions exhibit considerable noise, visible already in the small frequency range of Fig. 3.2. Naturally in QMC, the one-frequency objects are determined with greater accuracy than the two-frequency objects. But here the knowledge comes to our aid that the kernel functions go to zeros for high frequencies:¹ We may just replace the kernel functions in their asymptotic range by zeros, thus “cutting off” the noise.

For $K^{(1)}$ it is rather straightforward to find a cutoff condition: just replace the values fulfilling $|\omega| > 2\pi a/\beta$ by 0, for a reasonably chosen parameter a . In the case of $K^{(2)}$ a reliable method is to replace values with $|\omega(\nu - \omega)| < (2\pi b/\beta)^2(1 + c\delta_{\omega 0})$ by zero. $K^{(2),\nu 0}$ goes to zero considerably slower than $K^{(2),\nu\omega \neq 0}$ in some cases. Reasonable values for the cutoff parameters are printed in Tables 3.1.

Although at first the cutoff appears as a minor detail, it is in fact crucial for the whole procedure. While the error of the kernel functions can be considered statistical, it introduces a *systematic* error to the vertex. The best way to explain this circumstance is an example. Let us assume the function $K^{(1),ph}$ exhibits strong noise for larger values of ω then, e. g. $K^{(1),ph,\omega} = +0.5U$ and $K^{(1),ph,\omega+1} = -0.8U$. These two values are not correlated, but they have the effect, that the constant backgrounds of $F^{\nu\nu'\omega}$ and $F^{\nu\nu'\omega+1}$ are 50% too large and 80% too small, respectively. This is very problematic, because not only single points in frequency space have this error, but the whole ν - ν' plane deviates by the same value and hence, the error is correlated and leads to systematically wrong results. Since all kernel functions influence the vertex in different ways, it might be difficult to identify such errors in some cases.

Hence it is obviously inevitable to determine the kernel functions with high accuracy on the frequency interval, where they differ from zero.

3.1.2 Asymptotic replacement

Knowing the kernel functions with sufficient accuracy, it is straightforward to combine them to the asymptotic vertex by Eq. (2.28). It is, however, less obvious, in which region we may actually replace the full (“exact”) vertex by the asymptotic

¹Note that the finite asymptotic values of F originate, on the one hand, from the constant contribution U , and on the other hand, from the fact that we use *differences* of fermionic frequencies as bosonic arguments of the kernel functions.

	a	b	c
ph	10	10	5
\overline{ph}	20	10	5
pp	40	25	5

Table 3.1: The cutoff parameters used in our calculations of the Hubbard model. In the pp channel, a and b have to be chosen much larger due to the broadened shape of the respective kernel functions.

one. Again, studying the atomic limit is enlightening here. Formula 2.62 for the difference between the exact and the asymptotic vertex basically already provides a recipe. The decay $1/(\nu_1\nu_2\nu_3\nu_4)$ suggests to use the four-frequency product as the main criterion. The enhanced particle-hole contributions lead to a loosening of the condition near the particle-hole diagonals $\delta_{\omega 0}$ and $\delta_{\nu\nu'}$. Putting the above reasoning into a formula, we obtain

$$\left(\frac{\beta}{\pi}\right)^4 |\nu_1\nu_2\nu_3\nu_4| > l^4 |1 + \delta_{\nu_1\nu_2} + \delta_{\nu_1\nu_4} - \delta_{\nu_1\nu_2}\delta_{\nu_1\nu_4}|^4 \quad (3.1)$$

If the above condition is true, the asymptotic vertex can be used. Of course, a certain arbitrariness is inherent to the choice of the replacement parameter l , as well as the cutoff-parameters. Therefore the next subsection is dedicated to tests of the correctness of the parameters.

3.1.3 Tests of the correctness of parameters

The cutoff parameters can be checked by just looking at plots of $K^{(1)}$ and slices of $K^{(2)}$. Matters become more intricate with the replacement parameter l , however. One obvious check would be directly at the vertex F and from the regions where it matches the asymptotic vertex determine a reasonable value of l . But this method has two major drawbacks: First, F is a three-frequency object with a rather complex structure, such that direct inspection would require a lot of (human) effort. Second, the condition (3.1) generates a shape that strongly depends on the position in frequency space (see Fig. 3.3) and thus, even knowing where to apply the asymptotic vertex, it would be difficult to find out the replacement parameter.

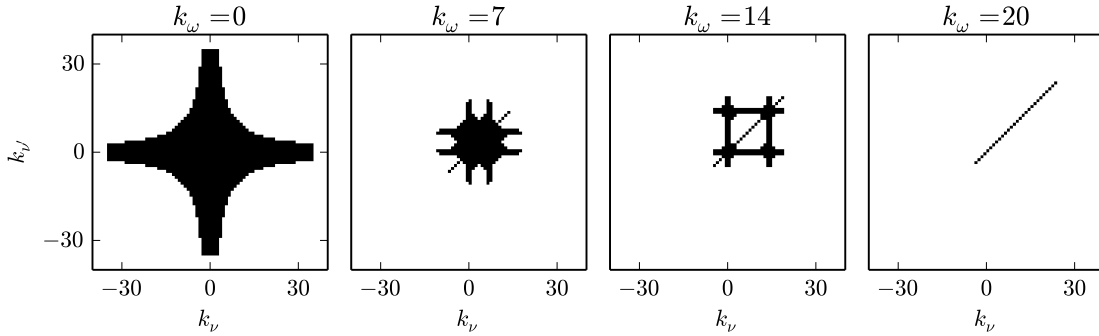


Figure 3.3: The asymptotic region (white) in the ν - ν' plane at various values of ω_{ph} , generated by condition (3.1).

A better way is to consider the susceptibility, summed over the fermionic frequencies. It has to be calculated for several values of the replacement parameter l and then decide at which l a kind of convergence is reached (see Fig. 3.4, left panel).

In our test case, ED data are present and we can also calculate the absolute error

$$E(l) = \sum_{\omega} |\Delta^{\omega}(l)| = \sum_{\omega} |\chi^{\omega}(l) - \chi_{ED}^{\omega}| \quad (3.2)$$

and take the value of l near to where it has its minimum (see Fig. 3.4, right panel). The peculiar behaviour of the absolute error, shown in the right panel of Fig. 3.4, can be explained by the curves shown in the right panel: At very low values of the replacement parameter the result (thin gray lines) is totally wrong, as expected if the asymptotics is used in non-asymptotic regions. With increasing of the replacement parameter, the result quickly converges to the correct solution from ED. An even higher value leads to the incorporation of more and more data from the full-QMC vertex that exhibits more noise, leading also to a slight worsening of the result, see the lower part of the left panel in Fig. 3.4

Since the minimum of the error with respect to l is rather flat, I use a value of $l = 10$, slightly to the right of the actual minimum at $l = 8$. This is done in order to ensure the correctness of the result.

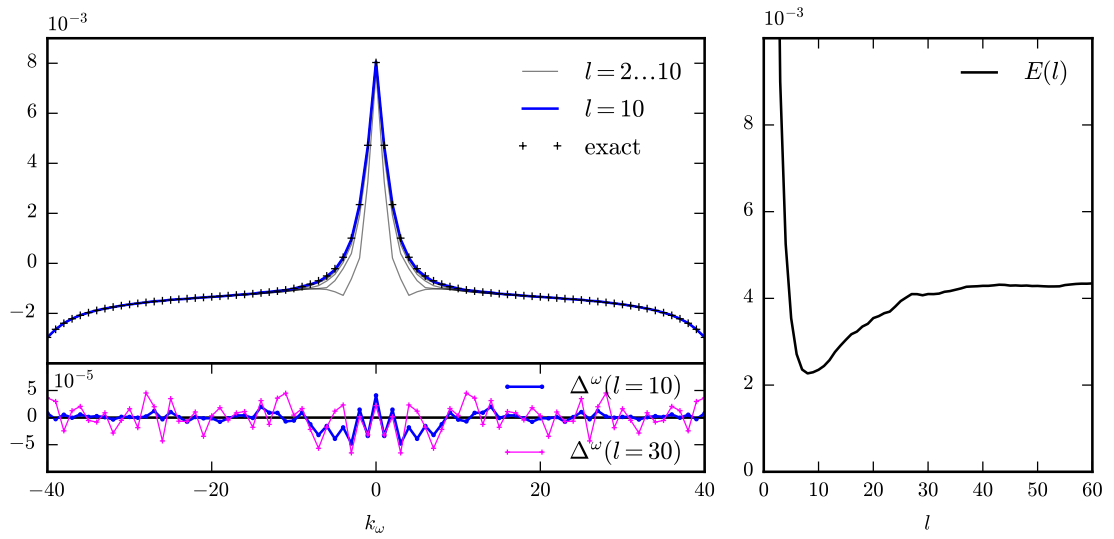


Figure 3.4: Left: Charge susceptibility from ED (crosses), and from QMC with asymptotics for various values of l (thin gray lines). The curve for the optimal replacement parameter $l = 10$ is the thick blue line. The lower left panel shows the deviation $\Delta^\omega(l)$ for $l = 10$ and $l = 30$. Right: Absolute error $E(l)$, Eq. (3.2), of the charge susceptibility in dependence on l .

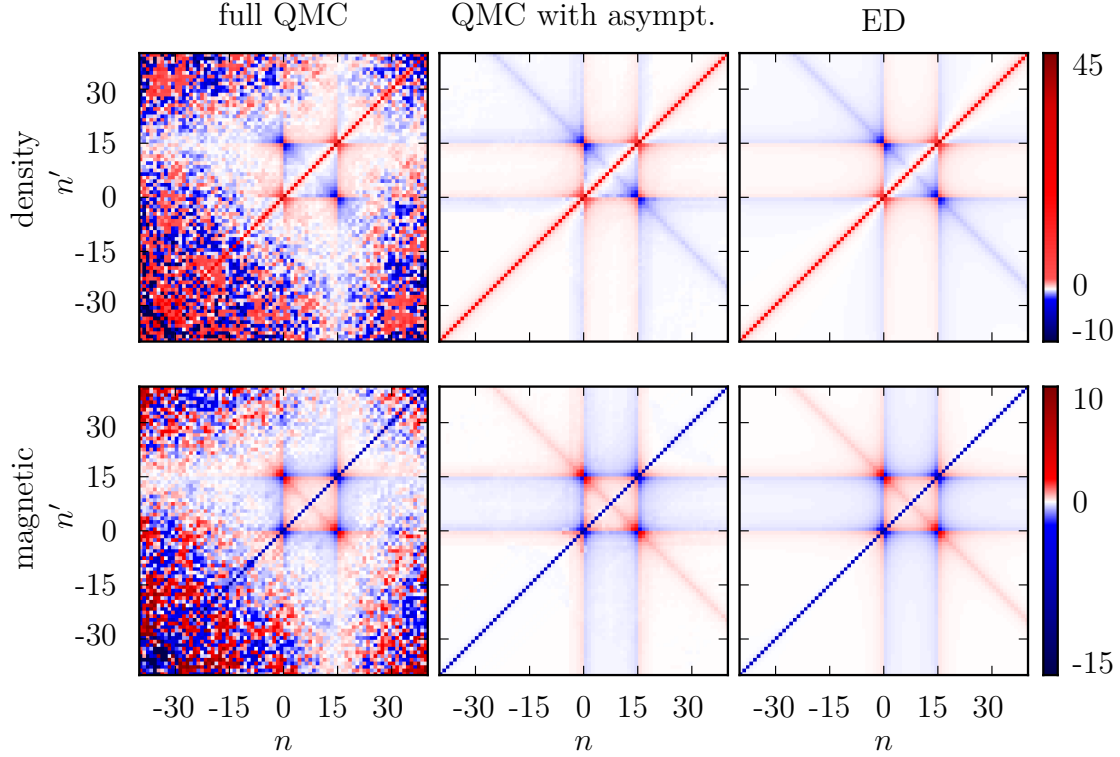


Figure 3.5: Full vertex F for the Hubbard model at $U=2D$ and $\beta=8/D$. The upper row shows the density channel, the lower row the magnetic channel. First column: QMC data without asymptotics, second row: QMC data combined with asymptotics, third row: ED reference data.

3.1.4 Calculations

Full vertex

Now we are able to perform actual calculations. First, the full vertex is shown in Fig. 3.5). It is immediately visible that the vertex with applied asymptotics exhibits less statistical noise than the original QMC vertex. The difference to the ED solution is very small and hardly visible.

The basic assumption that makes the application of the asymptotics possible, is that the difference of the full vertex and its purely asymptotic version goes to zero for high frequencies. In Fig. 3.6 we show that this is indeed the case for the Hubbard model under consideration.

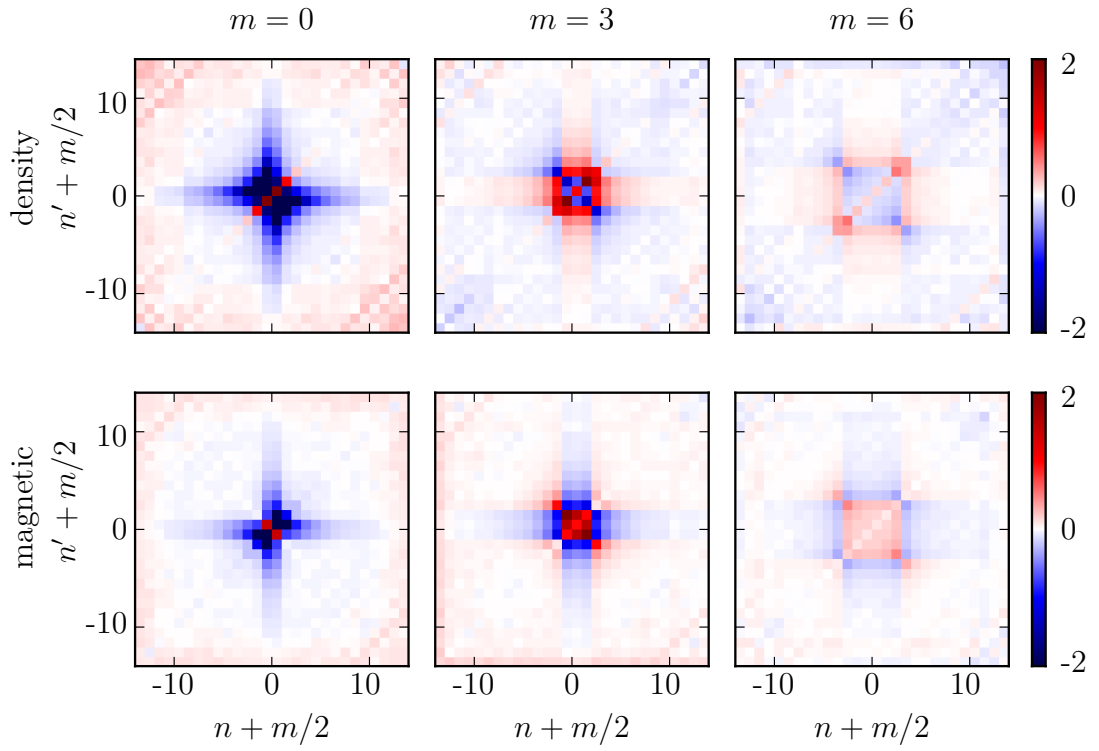


Figure 3.6: Difference of the ED vertex and the purely asymptotic vertex in the density and magnetic channels at different bosonic frequencies $\omega_m^{ph} = 2m\pi/\beta$.

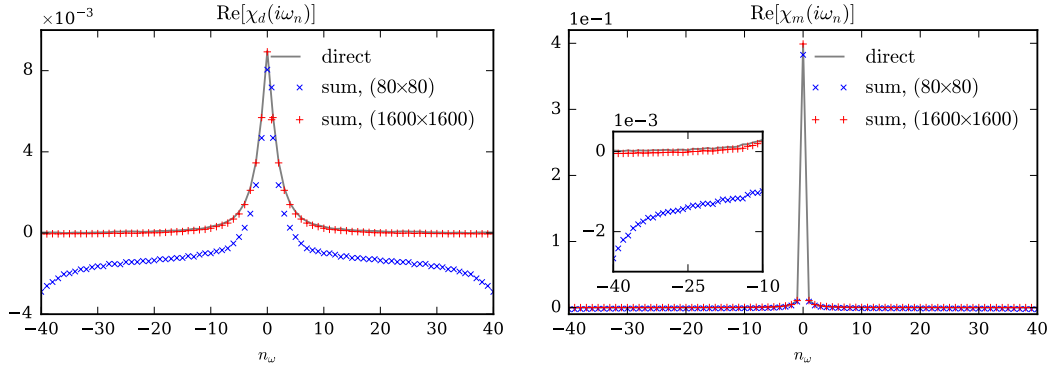


Figure 3.7: Physical susceptibility in the density (left) and magnetic channel (right). The gray curves are directly measured in QMC. (They are actually needed in order to calculate the kernel functions and serve as reference data.) The improvement due to extending the frequency box of the vertex from 80^2 to 1600^2 is visible as the difference between the blue (no vertex asymptotics) and red crosses (using the vertex asymptotics for getting a larger frequency box).

Physical susceptibility

In Sec. 3.1.3, the physical susceptibility was calculated by summing over a box of the same size as the original QMC data or the ED data in order to reproduce the results from there. However, the initial purpose of using vertex asymptotics was to enlarge the frequency box. Fig. 3.7 shows the improvement when using an extended frequency box for the vertex, which is possible thanks to vertex asymptotics.

Self-energy

Furthermore it is possible to calculate the the self-energy by means of the Schwinger-Dyson equation of motion, that is in the one-band case [14]

$$\Sigma(\nu) = \frac{Un}{2} - \frac{U^2}{\beta} \sum_{\nu'\omega} F_{\uparrow\downarrow}^{\nu\nu'\omega} G^{\nu'} G^{\nu-\omega} G^{\nu'-\omega}. \quad (3.3)$$

This corresponds to the principle of improved estimators and leads to a self-energy with reduced noise, see Fig. 3.8.

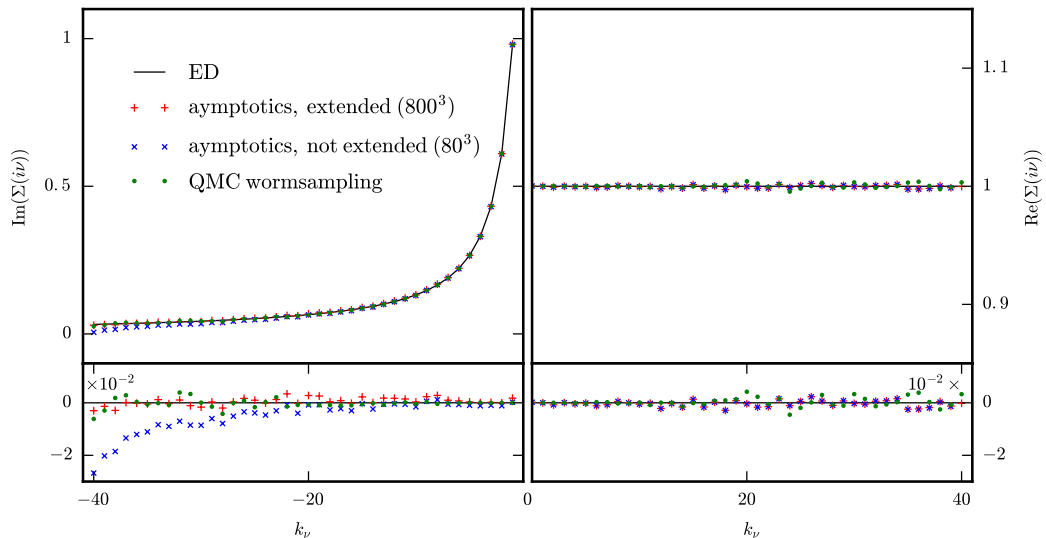


Figure 3.8: Self-energy $\Sigma(i\nu)$, as calculated with asymptotics and from QMC wormsampling.

Irreducible vertex

According to Eq. (1.76), the irreducible vertices in density and magnetic channels can be calculated by inverting the DMFT susceptibilities, which are matrices with respect to fermionic Matsubara frequencies, i. e.

$$\Gamma_{d/m} = [\chi_0]^{-1} - [\chi^{d/m}]^{-1}. \quad (3.4)$$

Since matrix inversion leads to enhanced noise, it is necessary to know the susceptibility very accurately, otherwise the structures of the vertex are not visible any more. The plots in Fig. 3.9 demonstrate that the asymptotics indeed fulfil their purpose very well. While it is important to replace as much of the original susceptibility by asymptotic data, the box size seems to be of minor impact in this case. (Nevertheless, the susceptibility was asymptotically extended to ten times the original size.)

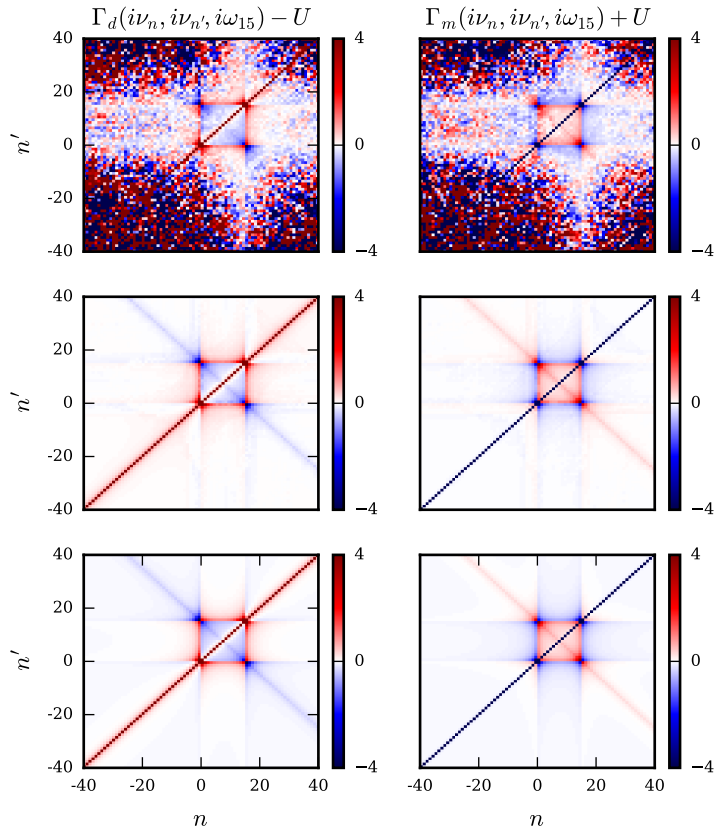


Figure 3.9: Irreducible vertices Γ_d (left column) and Γ_m (right column) in the density and magnetic ph -channel. First row: Calculated from QMC data without asymptotics, second row: calculated from QMC data with asymptotics, third row: ED results.

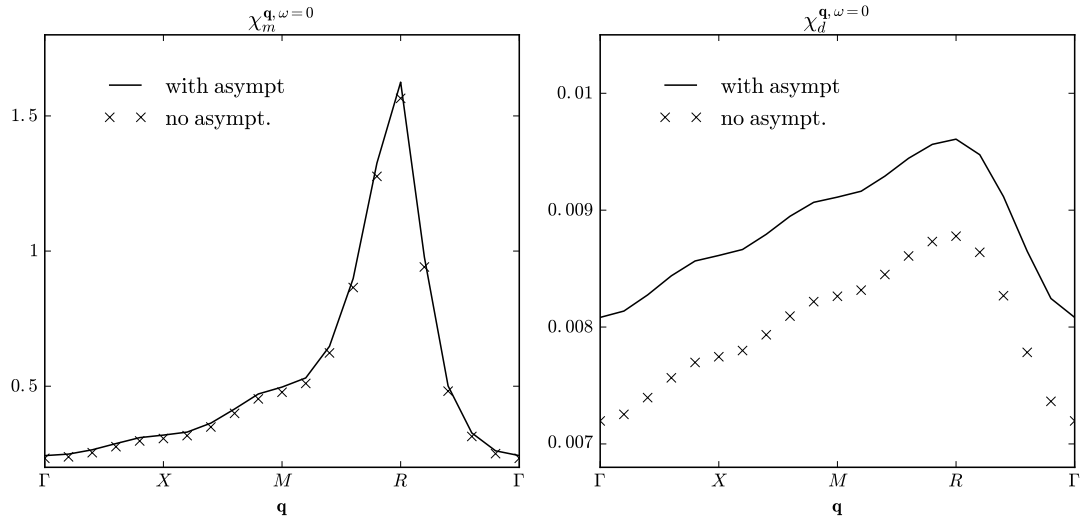


Figure 3.10: Momentum-dependent susceptibility in the magnetic (left) and density channel (right) at bosonic frequency 0 along a path that connects the symmetry points $\Gamma = (0, 0, 0)$, $X = (0, 0, \pi)$, $M = (0, \pi, \pi)$, $R = (\pi, \pi, \pi)$.

Momentum-dependent susceptibility

Assuming locality of the irreducible vertices, it is possible to calculate momentum-dependent susceptibilities, as described in Sec. 1.7.2. The momentum-dependent susceptibilities are of great importance, because they contain information about the preferred ordering of a system. In the example shown in Fig. 3.10, we notice an already pronounced maximum of the magnetic susceptibility at $\mathbf{q} = (\pi, \pi, \pi)$, which means that the system will go to antiferromagnetic ordering at lower temperatures. (For the system considered here, the critical inverse temperature would be $\beta_c^{\text{DMFT}} \approx 10.183$, see Fig. 3.11, and compare also Ref. [38]).

The corrections due to the usage of asymptotics are small and only of quantitative nature, slightly raising the values without changing the overall shape of the curve. This is consistent with the correction to the local susceptibility.

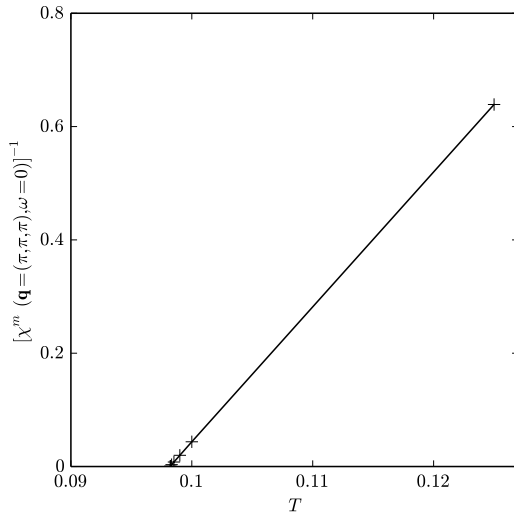


Figure 3.11: Inverse of the maximum of the \mathbf{q} -dependent susceptibility at $\mathbf{q} = (\pi, \pi, \pi)$ and $\omega = 0$ as a function of the temperature T . The Neel temperature is approximately $0.098D$.

3.2 Multi-band test case: SrVO_3

Strontium vanadate (SrVO_3) is a much more difficult case, because it cannot be described as a one-band system. At least the three t_{2g} orbitals have to be taken into account. Instead of density-density interaction, as in the one-band model considered above, one has to use Kanamori interaction to correctly model the system's behaviour. The interaction parameters are evaluated in constrained local density approximation (cLDA) to $U = 5\text{eV}$ and $J = 0.75\text{eV}$ [39, 40]. U' is then chosen as $U - 2J = 3.5\text{eV}$. The non-interacting band structure, which is necessary to perform DMFT and QMC calculations, is computed in density functional theory with generalized gradient approximation by `WIEN2K` [41]. The dispersion of the strongly correlated t_{2g} orbitals is obtained through projecting onto maximally localized Wannier functions by `WIEN2WANNIER` [42]. The DMFT and vertex calculations are then done with the package `W2DYNAMICS` [26, 43].

For the most general interaction, a three-band vertex would have $(2 \times 3)^4 = 1296$ spin-orbital components. (Every component is still a three-dimensional matrix in Matsubara frequency.) The Kanamori interaction reduces the number of non-zero

	a	b	c
ph	40	13	5
\overline{ph}	15	10	5
pp	200	25	5

Table 3.2: The cutoff parameters used in our calculations of SrVO₃. In the pp channel, a and b have to be chosen much larger due to the broadened shape of the respective kernel functions.

components to 126. Although this is a great reduction, there are still considerably more components than in the one-band case, where there were only 6. Due to this large number of components it takes significantly more computational effort to measure three-band vertices in QMC, which became possible only recently thanks to the worm sampling technique [30].

Whereas in the Hubbard test case finding the replacement parameter l was facilitated by the possibility of comparing to ED data, this is much more difficult in a “real” case like SrVO₃, where we have to rely solely on our QMC data. Another complication results from the fact, that in the three-band case also the two- and three-time two-particle Green’s functions can only be measured with less statistical accuracy. The cutoff of the kernel functions, merely a commodity for the Hubbard model calculations above, becomes a sheer necessity here. Otherwise, noise almost totally corrupts the data. Reasonable values for the cutoff parameters are printed in Tables 3.2.

One way to find a good value for the replacement parameter l is to compare the frequency-summed susceptibility to the one obtained from the two-time two-particle Green’s function. Since the latter can not show any finite-box deficiencies, the summation has to be performed over a reasonably large box. This implies that also these test calculations require considerably more time than in the case above, where the ED reference data themselves were obtained by summation over a small box. As reasonable value for the replacement parameter in SrVO₃ we find $l \sim 15$.

Full vertex

As above, an optical inspection of the full vertex F is interesting also in this case. Fig. 3.12 shows a slice of F at $\omega_{ph} = 15 \times 2\pi/\beta$. The reduction of statistical noise

is visible at first sight. Nevertheless also in the vertex with asymptotics applied, some noise is clearly visible. Indeed, one has to handle the cutoff of the kernel functions very carefully. A loose cutoff in, e.g. a $K^{(2)}$ -function quickly leads to “lines” appearing in the cross structure of F . On the other hand, cutting off too much will remove parts of the structure of the vertex. Hence one has to find well-balanced cutoff parameters in order to keep the statistical error at a minimum, while still not introducing systematic deviations.

In Fig. 3.13 the component with four equal band indices of the difference of the fully frequency dependent and the purely asymptotic vertex is shown. The noise level is much higher here than in the case of the Hubbard model (Fig. 3.6), because there we could subtract the asymptotic vertex from noise-free ED data, whereas here both the asymptotic and the full vertex exhibit noise. Although the difference goes to zero for high frequencies also in the case of SrVO_3 , this is happening much slower than in the Hubbard model considered before. We note however, that in the atomic limit, the difference of full and asymptotic vertex R consists of terms proportional to U^5 and U^6 , such that a slower decay of R is expected at stronger interaction. Considering that the local interaction in SrVO_3 is higher than in the Hubbard model with the parameters used above, we presume that the results found in the atomic limit, similarly hold for hybridizing systems.

Frequency-summed susceptibility

In Fig. 3.14 examples of frequency-summed susceptibilities in the density and magnetic channels are shown. Especially in the magnetic channel, one can see that these components are difficult to accurately measure in QMC. The value at $\omega = 0$, as calculated by summation of the original QMC data, greatly deviates from the respective value that was directly measured in QMC and which we assume to be correct. The reason for this might be, that the generalized susceptibility does not decay to zero within the original frequency box. If the summation is performed over a larger box, the result is gradually improved and however seems to converge towards the real value. This demonstrates the improvement brought about by the vertex asymptotics.

In regions of high bosonic frequency we observe that the values computed by

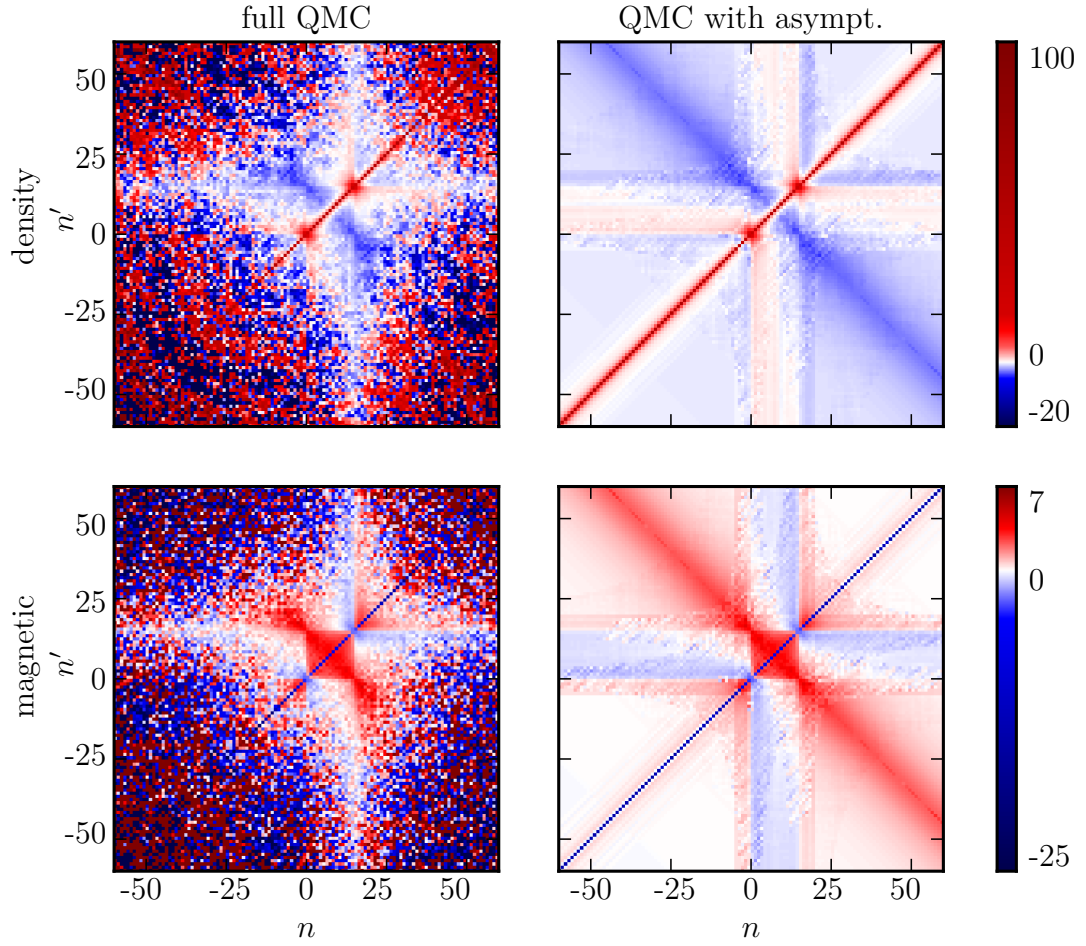


Figure 3.12: Full vertex $\text{Re}[F_{iii}^{d/m, \nu\nu'\omega_{15}}]$ with four times the same t_{2g} orbital. in density and magnetic channels. The left column shows the vertices as obtained from direct (full) QMC measurements for all frequencies; in the right column, the asymptotics were considered separately.

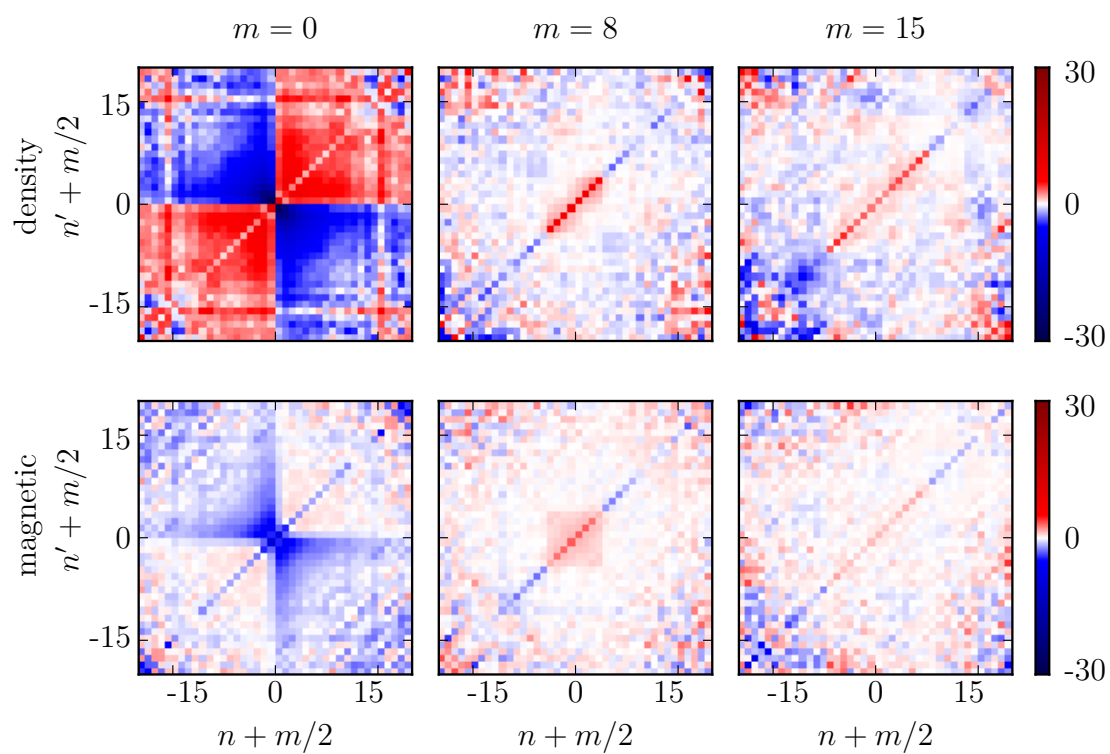


Figure 3.13: Difference between the full QMC vertex and purely asymptotic vertex for different bosonic frequencies $\omega_m = 2\pi m/\beta$.

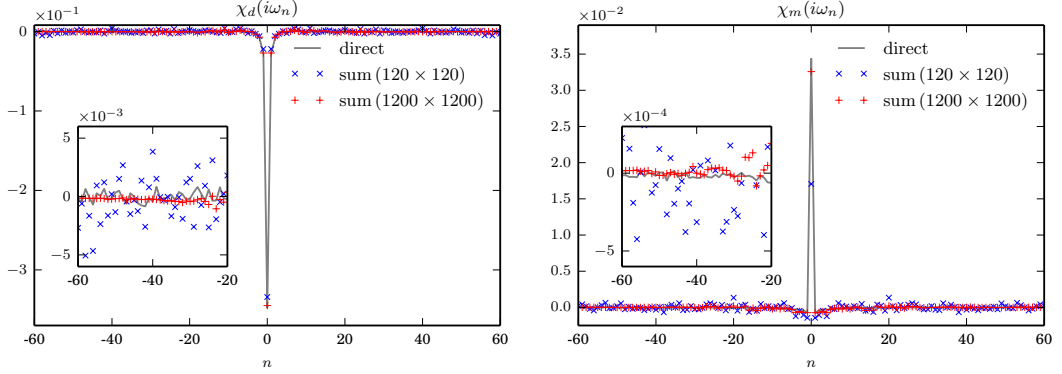


Figure 3.14: Frequency-summed susceptibilities χ_{ijj}^ω between two different t_{2g} orbitals in the density (left) and magnetic (right) channels.

summation over the asymptotically extended susceptibility exhibit even less noise than the ones obtained by direct QMC measurement.

Self-energy

It emerged to be a rather critical test to the asymptotics procedure to compute the self-energy by means of the Schwinger-Dyson equation of motion. For the multiband case, it is [33, 44]

$$\Sigma_a^\nu = \sum_{b,\nu'} \left[(U_{abbd} - U_{abdb}) G_b^{\nu'} + \frac{1}{\beta} \sum_{ce\omega} U_{abce} G_v^{\nu'-\omega} G_c^{\nu-\omega} G_e^{\nu'} F_{ebcd}^{\nu'\nu\omega} \right]. \quad (3.5)$$

In the upper panels of Fig. 3.15 it is visible, that the calculation without asymptotics (blue crosses) yields highly inaccurate values, even in the low-frequency region. This can be improved on, using a large vertex extended by its asymptotic form (red crosses); but still the accuracy of QMC with worm sampling and improved estimators [31] (green lines) is not reached. However, the situation drastically changes at higher frequencies, where the asymptotic vertex leads to a very smooth curve. The asymptotic behaviour of self-energies can be described as

$$\Sigma_{\text{asymptotic}}^\nu = \Sigma_0 + \frac{\Sigma_1}{i\nu}, \quad (3.6)$$

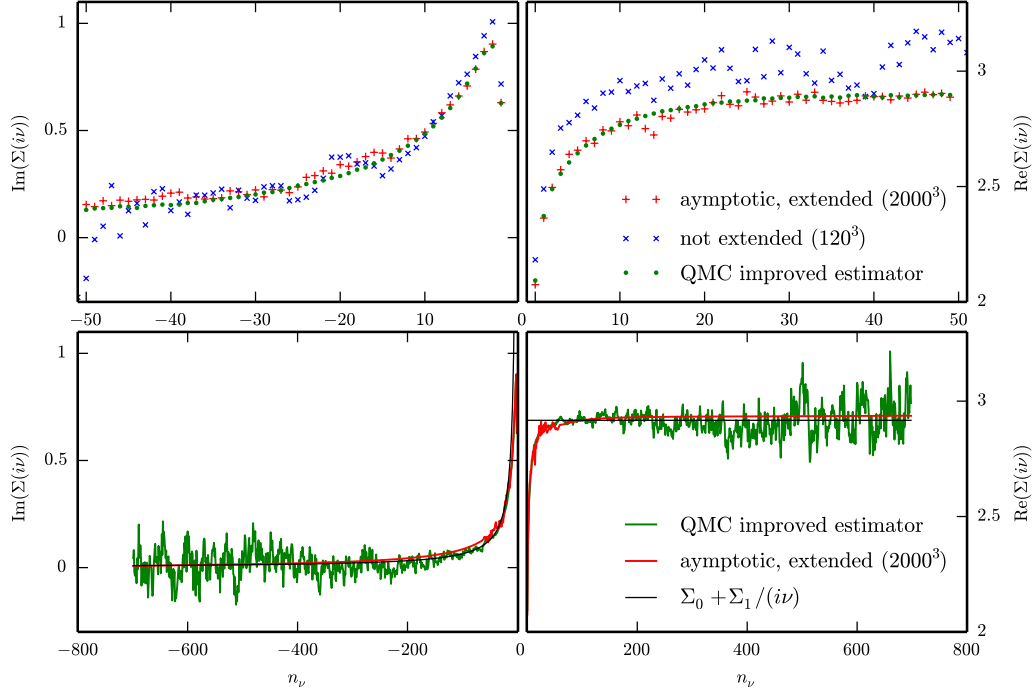


Figure 3.15: DMFT self-energy Σ^ν of SrVO_3 vs. Matsubara frequency index $n\nu$ at $\beta = 10\text{eV}^{-1}$. Left plots: Imaginary part on negative imaginary axis, right plots: real part on positive imaginary axis. The upper row shows the low-frequency region, the lower row shows a larger frequency range. The blue (red) crosses are the result obtained without (with) asymptotic extension of the vertex using 120^3 (1200^3) Matsubara frequencies, the green dots are obtained by QMC improved estimators with worm sampling. As a comparison, the black lines in the lower panel show the high-frequency self-energy calculated via its zeroth and first moment.

where the so-called *moments* Σ_0 and Σ_1 can be calculated directly from the one- and two-particle density matrix [45]. This asymptotic form of the self-energy (black line) is compared to the QMC improved estimator and Eq. (3.5) with vertex asymptotics for F in the lower panels of Fig. 3.15. Altogether, we observe that using the vertex asymptotics allows for calculating the self-energy through the Schwinger-Dyson Eq. (3.5) whereas otherwise this is not possible with good accuracy.

Chapter 4

Conclusion and outlook

In this work, the recently derived asymptotic form of the vertex [36, 35] was adapted in order to make it possible to calculate the occurring vertex kernel functions from local Green's functions. We further generalize the concept to multiple orbitals. Although in principle there exist several methods to calculate impurity Green's functions, we chose continuous-time quantum Monte Carlo. For calculating the required equal-time Green's functions we employ worm sampling. We prove by means of analytic calculations that the concept works in the atomic limit. Then we show that it also works in practice by applying it to specific problems. First, a one-band Hubbard model is investigated, subsequently we show that our method also works for multiple bands with general interaction, using SrVO_3 as an example material.

It is appropriate to add a word of caution to this summary: Usually, in QMC less measurements result in a higher statistical uncertainty of the result. The errors of adjacent Matsubara matrix elements are uncorrelated. When using vertex asymptotics, the statistical error is much more difficult to quantify, but in any case, the errors are not uncorrelated any more. Thus one can get a very smooth curve, e. g. for the physical susceptibility, seemingly without any noise and yet its values deviate from the real values. This danger can only be circumvented by measuring the asymptotics with highest possible precision. Then the quality of the result is truly very much improved.

In the near future we are going to calculate vertices and their asymptotics for the cuprate $\text{HgBa}_2\text{CuO}_4$ at various fillings and low temperatures in order to perform

precise calculations in dynamical vertex approximation. The aim of this ongoing project is to get new insights into the intriguing magnetic properties of the material and their interconnection to its mechanism of high-temperature superconductivity.

Appendix A

Frequency notations

In contrast to one-particle Green's functions, there are several ways of Fourier transforming two-particle Green's functions or susceptibilities. The most basic way would be to use four fermionic Matsubara frequencies and write

$$\chi_{ijkl}^{\nu_1, \nu_2, \nu_3, \nu_4} = \int d\tau_1 d\tau_2 d\tau_3 d\tau_4 \chi_{ijkl}(\tau_1, \tau_2, \tau_3, \tau_4) e^{i\nu_1\tau_1 - i\nu_2\tau_2 + i\nu_3\tau_3 - i\nu_4\tau_4}. \quad (\text{A.1})$$

However, already in equation (1.19) we saw that energy conservation effectively reduces the number of Matsubara frequencies by one. Thus, we can choose three (one bosonic and two fermionic) frequencies fulfilling the constraint

$$\nu_1 - \nu_2 + \nu_3 - \nu_4 = 0. \quad (\text{A.2})$$

Obviously, this permits a variety of choices and consequently there exist several conventions. Furthermore it is convenient to define different notations for the three scattering channels (particle-particle, particle-hole and transverse particle-hole). To denote the channel, we use subscripts pp , ph and \overline{ph} . If there is no subscript, this means that the frequency belongs to the particle-hole notation, e. g. $\nu \equiv \nu_{ph}$. Conventionally, ω refers to a bosonic and ν to a fermionic Matsubara frequency. The following equations define the particle-particle, particle-hole, and transversal

particle-hole notation for the four fermionic frequencies ν_1 , ν_2 , ν_3 , and ν_4 :

$$\nu_1 = \nu_{pp} \qquad = \nu_{ph} \qquad = \nu_{\bar{ph}} \qquad (\text{A.3})$$

$$\nu_2 = \omega_{pp} - \nu'_{pp} \qquad = \nu_{ph} - \omega_{ph} \qquad = \nu'_{\bar{ph}} \qquad (\text{A.4})$$

$$\nu_3 = \omega_{pp} - \nu_{pp} \qquad = \nu'_{ph} - \omega_{ph} \qquad = \nu'_{\bar{ph}} - \omega_{\bar{ph}} \qquad (\text{A.5})$$

$$\nu_4 = \nu'_{pp} \qquad = \nu'_{\bar{ph}} \qquad = \nu_{\bar{ph}} - \omega_{\bar{ph}}. \qquad (\text{A.6})$$

The susceptibility $\chi_{ijkl}^{\nu_1, \nu_2, \nu_3, \nu_4}$ is then written with only three indices, i. e.

$$\chi_{ijkl}^{\nu\nu'\omega} = \int d\tau_1 d\tau_2 d\tau_3 \chi_{ijkl}(\tau_1, \tau_2, \tau_3, \tau_4) e^{i\nu(\tau_1 - \tau_2) + i\nu'(\tau_3 - \tau_4) + i\omega(\tau_2 - \tau_3)} \qquad (\text{A.7})$$

in the particle-hole channel and analogous in the other channels.

The above definitions make it possible to express all channel-specific frequencies in terms of each of the other notations (see also Ref. [37]):

$$\nu_{pp} = \nu_{ph} = \nu_{\bar{ph}} \qquad (\text{A.8})$$

$$\nu'_{pp} = \nu'_{ph} = \nu_{\bar{ph}} - \omega_{\bar{ph}} \qquad (\text{A.9})$$

$$\omega_{pp} = \nu_{ph} + \nu'_{ph} - \omega_{ph} = \nu_{\bar{ph}} + \nu'_{\bar{ph}} - \omega_{\bar{ph}} \qquad (\text{A.10})$$

$$\omega_{ph} = \nu_{pp} + \nu'_{pp} - \omega_{pp} = \nu_{\bar{ph}} - \nu'_{\bar{ph}} \qquad (\text{A.11})$$

$$\nu'_{\bar{ph}} = \nu_{ph} - \omega_{ph} = \omega_{pp} - \nu'_{pp} \qquad (\text{A.12})$$

$$\omega_{\bar{ph}} = \nu_{ph} - \nu'_{ph} = \nu_{pp} - \nu'_{pp} \qquad (\text{A.13})$$

Bibliography

- [1] N. F. Mott. “Metal-Insulator Transition”. In: *Rev. Mod. Phys.* 40 (4 1968), pp. 677–683. DOI: 10.1103/RevModPhys.40.677.
- [2] J. G. Bednorz and K. A. Müller. “Possible highTc superconductivity in the Ba-La-Cu-O system”. In: *Zeitschrift für Physik B Condensed Matter* 64.2 (1986), pp. 189–193. ISSN: 1431-584X. DOI: 10.1007/BF01303701.
- [3] W. Kohn and L. J. Sham. “Self-Consistent Equations Including Exchange and Correlation Effects”. In: *Phys. Rev.* 140 (4A 1965), pp. 1133–1138. DOI: 10.1103/PhysRev.140.A1133.
- [4] Max Born and Robert Oppenheimer. “Zur quantentheorie der molekeln”. In: *Annalen der Physik* 389.20 (1927), pp. 457–484.
- [5] K. Held. “Electronic structure calculations using dynamical mean field theory”. In: *Advances in Physics* 56.6 (2007), pp. 829–926. DOI: 10.1080/00018730701619647.
- [6] J. Hubbard. “Electron Correlations in Narrow Energy Bands”. In: *Proceedings of the Royal Society of London A: Mathematical, Physical and Engineering Sciences* 276.1365 (1963), pp. 238–257. ISSN: 0080-4630. DOI: 10.1098/rspa.1963.0204.
- [7] Junjiro Kanamori. “Electron Correlation and Ferromagnetism of Transition Metals”. In: *Progress of Theoretical Physics* 30.3 (1963), pp. 275–289. DOI: 10.1143/PTP.30.275.
- [8] Antoine Georges, Luca de’ Medici, and Jernej Mravlje. “Strong electronic correlations from Hund’s coupling”. In: *Annual Review of Condensed Matter Physics* 4.137-178 (2013). DOI: 10.1146/annurev-conmatphys-020911-125045.

- [9] P. W. Anderson. “Localized Magnetic States in Metals”. In: *Phys. Rev.* 124 (1 1961), pp. 41–53. DOI: 10.1103/PhysRev.124.41.
- [10] A A Abrikosov et al. *Methods of quantum field theory in statistical physics*. New York, NY: Dover, 1975.
- [11] G. Rickayzen. *Green’s functions and condensed matter*. Academic Press Inc., 1980.
- [12] A. Zagoskin. *Quantum Theory of Many-Body Systems: Techniques and Applications*. Graduate Texts in Contemporary Physics. Springer New York, 1998. ISBN: 9780387983844.
- [13] David James Thouless, H S W Massey, and Keith A Brueckner. *The quantum mechanics of many-body systems; 1st ed.* New York, NY: Academic Press, 1961.
- [14] Georg Rohringer. *New routes towards a theoretical treatment of nonlocal electronic correlations*. Dissertation Technische Universität Wien. 2013.
- [15] G. Rohringer, A. Valli, and A. Toschi. “Local electronic correlation at the two-particle level”. In: *Phys. Rev. B* 86 (12 2012), p. 125114. DOI: 10.1103/PhysRevB.86.125114.
- [16] G. C. Wick. “The Evaluation of the Collision Matrix”. In: *Phys. Rev.* 80 (2 1950), pp. 268–272. DOI: 10.1103/PhysRev.80.268.
- [17] Walter Metzner and Dieter Vollhardt. “Correlated Lattice Fermions in $d = \infty$ Dimensions”. In: *Phys. Rev. Lett.* 62 (3 1989), pp. 324–327. DOI: 10.1103/PhysRevLett.62.324.
- [18] E. Müller-Hartmann. “The Hubbard model at high dimensions: some exact results and weak coupling theory”. In: *Zeitschrift für Physik B Condensed Matter* 76.2 (1989), pp. 211–217. ISSN: 1431-584X. DOI: 10.1007/BF01312686.
- [19] Antoine Georges and Gabriel Kotliar. “Hubbard model in infinite dimensions”. In: *Phys. Rev. B* 45 (12 1992), pp. 6479–6483. DOI: 10.1103/PhysRevB.45.6479.

- [20] Michel Caffarel and Werner Krauth. “Exact diagonalization approach to correlated fermions in infinite dimensions: Mott transition and superconductivity”. In: *Phys. Rev. Lett.* 72 (10 1994), pp. 1545–1548. DOI: 10.1103/PhysRevLett.72.1545.
- [21] J. E. Hirsch and R. M. Fye. “Monte Carlo Method for Magnetic Impurities in Metals”. In: *Phys. Rev. Lett.* 56 (23 1986), pp. 2521–2524. DOI: 10.1103/PhysRevLett.56.2521.
- [22] Emanuel Gull et al. “Continuous-time Monte Carlo methods for quantum impurity models”. In: *Rev. Mod. Phys.* 83 (2 2011), pp. 349–404. DOI: 10.1103/RevModPhys.83.349.
- [23] A N Rubtsov and A I Lichtenstein. “Continuous-time quantum Monte Carlo method for fermions: Beyond auxiliary field framework”. In: *Journal of Experimental and Theoretical Physics Letters* 80.1 (2004), pp. 61–65. ISSN: 1090-6487. DOI: 10.1134/1.1800216.
- [24] Philipp Werner et al. “Continuous-Time Solver for Quantum Impurity Models”. In: *Phys. Rev. Lett.* 97 (7 2006), p. 076405. DOI: 10.1103/PhysRevLett.97.076405.
- [25] Philipp Werner and Andrew J. Millis. “Hybridization expansion impurity solver: General formulation and application to Kondo lattice and two-orbital models”. In: *Phys. Rev. B* 74 (15 2006), p. 155107. DOI: 10.1103/PhysRevB.74.155107.
- [26] Markus Wallerberger. *w2dynamics: continuous time quantum Monte Carlo calculations of one- and two-particle propagators*. Dissertation Technische Universität Wien. 2016.
- [27] Patrik Gunacker. *Diagrammatic quantum Monte-Carlo with worm-sampling*. Diplomarbeit Technische Universität Wien. 2014.
- [28] Nicholas Metropolis et al. “Equation of State Calculations by Fast Computing Machines”. In: *The Journal of Chemical Physics* 21.6 (1953), pp. 1087–1092. DOI: 10.1063/1.1699114.
- [29] W. K. Hastings. “Monte Carlo Sampling Methods Using Markov Chains and Their Applications”. In: *Biometrika* 57.1 (1970), pp. 97–109. ISSN: 00063444.

- [30] P. Gunacker et al. “Continuous-time quantum Monte Carlo using worm sampling”. In: *Phys. Rev. B* 92 (15 2015), p. 155102. DOI: 10.1103/PhysRevB.92.155102.
- [31] P. Gunacker et al. “Worm-improved estimators in continuous-time quantum Monte Carlo”. In: *Phys. Rev. B* 94 (12 2016), p. 125153. DOI: 10.1103/PhysRevB.94.125153.
- [32] A. Toschi, A. A. Katanin, and K. Held. “Dynamical vertex approximation: A step beyond dynamical mean-field theory”. In: *Phys. Rev. B* 75 (4 2007), p. 045118. DOI: 10.1103/PhysRevB.75.045118.
- [33] Anna Galler et al. “Ab initio dynamical vertex approximation”. In: *Phys. Rev. B* 95 (11 2017), p. 115107. DOI: 10.1103/PhysRevB.95.115107.
- [34] Jan Kune š. “Efficient treatment of two-particle vertices in dynamical mean-field theory”. In: *Phys. Rev. B* 83 (8 2011), p. 085102. DOI: 10.1103/PhysRevB.83.085102.
- [35] Gang Li et al. “Efficient implementation of the parquet equations – role of the reducible vertex function and its kernel approximation”. In: *Phys. Rev. B* 93 (2016), p. 195134.
- [36] N. Wentzell et al. *High-frequency asymptotics of the vertex function: diagrammatic parametrization and algorithmic implementation*. 2016. eprint: arXiv:1610.06520.
- [37] J. Kaufmann, P. Gunacker, and K. Held. “Continuous-time quantum Monte Carlo calculation of multi-orbital vertex asymptotics”. 2017 (in preparation).
- [38] T. Schäfer et al. “Quantum criticality with a twist - interplay of correlations and Kohn anomalies in three dimensions”. 2016. URL: <http://arxiv.org/abs/1605.06355>.
- [39] A. Sekiyama et al. “Mutual Experimental and Theoretical Validation of Bulk Photoemission Spectra of $\text{Sr}_{1-x}\text{Ca}_x\text{VO}_3$ ”. In: *Phys. Rev. Lett.* 93.15 (2004), p. 156402. DOI: 10.1103/PhysRevLett.93.156402.
- [40] I. A. Nekrasov et al. “Momentum-resolved spectral functions of SrVO_3 calculated by LDA + DMFT”. In: *Phys. Rev. B* 73 (15 2006), p. 155112. DOI: 10.1103/PhysRevB.73.155112.

- [41] Karlheinz Schwarz and Peter Blaha. “Solid state calculations using WIEN2k”. In: *Computational Materials Science* 28.2 (2003). Proceedings of the Symposium on Software Development for Process and Materials Design, pp. 259–273. ISSN: 0927-0256. DOI: [http://dx.doi.org/10.1016/S0927-0256\(03\)00112-5](http://dx.doi.org/10.1016/S0927-0256(03)00112-5).
- [42] Jan Kuneš et al. “Wien2wannier: From linearized augmented plane waves to maximally localized Wannier functions”. In: *Computer Physics Communications* 181.11 (2010), pp. 1888–1895. ISSN: 0010-4655. DOI: <http://dx.doi.org/10.1016/j.cpc.2010.08.005>.
- [43] N. Parragh et al. “Conserved quantities of $SU(2)$ -invariant interactions for correlated fermions and the advantages for quantum Monte Carlo simulations”. In: *Phys. Rev. B* 86 (15 2012), p. 155158. DOI: [10.1103/PhysRevB.86.155158](https://doi.org/10.1103/PhysRevB.86.155158).
- [44] Karsten Held. “Dynamical Vertex Approximation”. In: *DMFT at 25: Infinite Dimensions*. (Forschungszentrum Jülich, 2014). Ed. by E. Pavarini et al. Reihe Modeling and Simulation, Vol. 4.
- [45] Xin Wang, Hung The Dang, and Andrew J. Millis. “High-frequency asymptotic behavior of self-energies in quantum impurity models”. In: *Phys. Rev. B* 84 (7 2011), p. 073104. DOI: [10.1103/PhysRevB.84.073104](https://doi.org/10.1103/PhysRevB.84.073104).

Acknowledgements

First and foremost, I would like to thank Karsten Held. It was both an honour and a great opportunity for me to study and work under his supervision and thus taking part in his tremendous knowledge of physics. He also made it possible for me to visit Andrey Katanin at the Institute of Metal Physics in Ekaterinburg, whom I also want to thank herewith for the great hospitality and inspiring discussions, which made my stay very enjoyable and productive.

I owe deep gratitude to my supervisor Patrik Gunacker. Clearly this work would not have been possible without him. Patrik introduced me to the basics of our research, and he taught me a lot of valuable programming skills. Furthermore he always made sure that my projects went into the right direction, and without his patient explanations I would still not be able to use w2dynamics.

Partly my work was in connection with the ab-initio D Γ A project, and in this context I want to thank Anna Galler and Jan Tomczak for explaining to me both the code and the formulas, and for many times providing useful help. I am also very grateful to Thomas Schäfer and Tin Ribic, who taught me a lot about DMFT, D Γ A and theoretical physics in general. Moreover I had many fruitful discussions with Patrick Chalupa, Petr Igoshev, Oleg Janson, Anna Kauch, Jan Kunes, Gang Li, Marie-Therese Philipp, Vladimir Protsenko, Petra Pudleiner, Liang Si, Daniel Springer, Patrik Thunström, Alessandro Toschi, Michael Wais, Markus Wallerberger, Clemens Watzenböck, and Nils Wentzell.

Besides these, I want to thank my friends and former colleagues for keeping up my spirit in times when this was necessary, and for enjoyable lunch and coffee breaks. With you, the Freihaus is a really nice place to work at.

Last, but not least, I want to express my deepest gratitude to my family and, in particular, to my parents. Without your unconditional generosity and support, I would not have been able to study in the way I did. Although I was at times not very responsive during the last months, you were always there for me when I needed your help.